frontiers in Physics

TYPE Original Research
PUBLISHED 28 August 2026
DOI 10.3389/fphy.2026.1870780

OPEN ACCESS

EDITED BY
Shrikaant Kulkarni,
Victorian Institute of Teaching, Australia

REVIEWED BY
Swarup Ghosh,
SR University, India
Anupam Behal,
Rajiv Gandhi Memorial Government College, India

*CORRESPONDENCE
Mohammed Abu-Jafar,
mabujafar@najah.edu

RECEIVED 01 May 2026
REVISED 22 June 2026
ACCEPTED 31 July 2026
PUBLISHED 28 August 2026

CITATION
Shtaiwi D, Abu-Jafar M, Hosen A and Masri H (2026) First-principles investigation of $YXMnH_6$ (X = Hg, Zn) complex hydrides: structural, electronic, optical, mechanical, and thermodynamic insights for H_2 storage efficiency.
Front. Phys. 14:1870780.
doi: 10.3389/fphy.2026.1870780

First-principles investigation of $YXMnH_6$ (X = Hg, Zn) complex hydrides: structural, electronic, optical, mechanical, and thermodynamic insights for H_2 storage efficiency

Doha Shtaiwi[1], Mohammed Abu-Jafar[1]*, Asif Hosen[2] and Hasan Masri[1]

[1]Department of Physics, An-Najah National University, Nablus, Palestine, [2]Department of Materials Science and Engineering, Khulna University of Engineering & Technology (KUET), Khulna, Bangladesh

This paper explores the structural, electronic, mechanical, optical, and thermodynamic characteristics of complex hydrides $YXMnH_6$ (X = Hg, Zn) to be used in hydrogen storage. The investigation is carried out through first principles calculations. Both compounds are dynamically and thermally stable, as indicated by the lack of negative frequencies in phonon dispersion calculations as well as being confirmed by AIMD simulations at room temperature with minimal fluctuations and no structural degradation. Electronic property-based $YHgMnH_6$ and $YZnMnH_6$ compounds exhibit semiconducting behavior, with indirect band gaps of 1.445 eV using PBE-GGA (1.826 eV using mBJ-GGA), and 1.555 eV using PBE-GGA (2.548 eV using mBJ-GGA), respectively. Its structural features indicate that $YHgMnH_6$ is characterized by the largest lattice constant (6.8623 Å) as compared to $YZnMnH_6$ (6.6506 Å), as mercury has a higher atomic radius than zinc. According to the Born stability criterion, both compounds are verified to be mechanically stable. 1t is also shown that $YZnMnH_6$ has a high Young's modulus and is appropriate for uses requiring hardness and resistance to deformation. Common optical property analysis indicates strong optical response of the ultraviolet region on both compounds; thus, they are good candidates in photovoltaic and optoelectronic applications. The hydrogen storage contents are estimated at 1.73 wt% of $YHgMnH_6$ and 2.81 wt% of $YZnMnH_6$. In general, these findings suggest that $YXMnH_6$ (X = Hg, Zn) complex hydrides are versatile substances and have the potential to be used in hydrogen storage systems and clean technologies. Further research will be in the field of experimental establishment of $YXMnH_6$ (X = Hg, Zn) in order to verify existing results and further study its energy applications.

KEYWORDS
AIMD, dynamical stability, hydrogen storage capacity, mechanical stability, optical, thermodynamic

1 Introduction

Over the past few decades, the world has experienced massive pressure on its energy resources, which is attributed to increasing human population, industrial development,

powering transportation, and improvement of living standards. This has been made possible by the fossil fuels of oil, natural gas, and coal that have facilitated this growth in a number of years. However, high reliance on these nonrenewable resources is also a high dependency with regard to the management of economic growth and environmental sustainability [1]. The fossil fuels cause large-scale CO_2 emissions of nearly 72% of all greenhouse gases, air pollution, and climate change and are expected to decline substantially in the coming few decades [2]. The existing estimates have indicated that the world oil reserves can just last up to 41 years so, the world is in dire need of making attempts to discover alternative forms of energy that will provide energy security [3]. As an effort to overcome such fears, renewable energy sources such as solar [4], wind, tidal, hydroelectricity, and geothermal energy have received a lot of attention [5, 6]. These are highly endowed resources that emit relatively lower carbon gases in comparison to conventional fuels. However, complexity is one of the biggest issues with most of the systems that are based on renewables, which are intrinsically limited to intermittency, storage issues, and variation in the efficiency of energy conversion [7]. As a result, the introduction of renewables into the global energy system must use an efficient, high-capacity energy carrier.

Hydrogen (H_2) has proved to be a major contributor to this change, and it will offer a clean, sustainable, and multi-purpose power supply. When used, H_2 gas gives out only water vapor, and the gravimetric energy density of this substance is 122 kJ/g, approximately 2.75 times that of gasoline [8]. However, H_2 has challenges related to low volumetric energy density; it is a big problem for safe, efficient, and compact storage [9]. Despite the fact that hydrogen is the most common element in the universe [10], molecular H_2 does not naturally occur on the earth and must be created using hydrogen-containing materials, further underlining the fact that hydrogen is an energy carrier (not a primary fuel). In order to utilize hydrogen as an alternative to the traditional fossil fuels, much needs to be done on storage technologies to ensure it has been made safe, efficient, compact, and cost-effective and stored either in compressed gas, liquid, or solid form. This is required in order to enable the mass adoption of hydrogen vehicles and a renewable energy transformation [11]. Among the various storage strategies, solid-state hydrogen storage is therefore one of the most promising and effective ways of storing it. In this case, hydrogen is incorporated into solid materials, including graphene, nanosheets, metal hydride, and perovskite-type hydride, in order to ensure that it can be stored in a compact and much-controlled manner [12]. This form of solid phase can both increase storage capacity and increase safety since less risk is needed in terms of leakages and high pressure. Consequently, solid-state hydrides have gained much interest in the framework of their applications in the transport sector and portables and stationary energy.

Perovskite hydride types have been found to be possible for hydrogen storage due to the elastic nature of their structure, their chemical composition can be modified, and they are multifunctional. The hydrides of simple perovskite of type ABX_3 are researched well, where the cations are A (alkaline earth metal such as Ca or Be), B (transition metal such as Mn or Mg), and X (anion hydrogen) [13]. B. Gheboulig et al. have studied $XCaH_3$ (X = Cs, and Rb) and have reported calculated lattice parameters agree with previous calculations and experimental data, as well as being structurally stable [14]. The structural, elastic, ultrasonic, and thermodynamic characteristics of $BaLiH_3$, $SrLiH_3$, and $CaLiH_3$ under pressures within the generalized gradient approximation were investigated by M. Abdul Hadi Shahet et al. [15]. It has been shown that perovskite-type hydrides of the sodium-based $NaXH_3$ (where X = Co, Fe, or Mn) have metallic properties and are thermodynamically and mechanically stable; $NaMnH_3$ has the maximum gravimetric storage capacity (3.74 wt%) [16]. The physical characteristics of lithium-based $LiAH_3$ (A = Sc, Ti, and V) show that $LiScH_3$ is brittle, but $LiTiH_3$ and $LiVH_3$ are ductile. The hydrides $LiScH_3$ have the largest gravimetric ratio, 5.7 wt%, according to their calculated hydrogen storage capabilities [17].

In recent studies, there has been a renewed interest in the research of the so-called double perovskite-based hydrides ($A_2BB'H_6$), due to several favorable advantageous properties, including tunable band gaps, high hydrogen content, mechanical robustness, excellent thermodynamic stability, and a wide range of optoelectronic applications. For example, the most suitable material for H_2 storage is $LiCaCoH_6$, according to a study by Asif et al. [18] on the possible use of $MCaM'H_6$ (M = Li, Na; M' = Co, Rh, Ir) as a solid-state hydrogen store. These hydrides were predicted to have hydrogen storage capacities of 5.40, 3.38, 2.47, 4.72, 3.52, and 2.31 wt%, respectively. The study found that $MCaM'H_6$ materials are mechanically brittle, dynamically stable, and exhibit indirect semimetallic behavior. The complex hydrides $ZBaGaH_6$ (Z = K, Rb, and Cs) have also shown remarkable efficiency; the hydrogen storage capacities for $KBaGaH_6$, $RbBaGaH_6$, and $CsBaGaH_6$ are found to be 2.40 wt%, 2.03 wt%, and 1.75 wt%, respectively. In the UV spectrum, $KBaGaH_6$ has the maximum optical activity [19]. For effective solid-state hydrogen storage materials, a variety of simple and complex hydrides have been theoretically studied, including $ZrNiH_3$ [20], $MgCoH_3$ [21], Q_2FeH_5 (Q = Mg, Ca, Sr) [22], Mg_2CaGeH_6 [23], A_2BH_6 (A = K, Rb; B = Ge, Sn) [24], Rb_2XYH_6 [25], $KSrIrH_6$ [26], and $KBaMH_6$ (M = Co, Rh, Ir) [27].

First-principles DFT modelling has become an especially useful approach in the contemporary search for useful solid-state materials to store hydrogen, filtering between hydrides and predicting their stability, phonon dynamics, and hydrogen release characteristics. As the interest of the present study is to obtain lightweight Hydrides of hydrogen-rich compounds with adjustable performances in regard to electronic and thermodynamic properties, the two new materials, $YXMnH_6$ (X = Hg, Zn), are developed as the basis of this research. However, these complex hydrides are not experimentally or theoretically investigated, and thus there is a gap in literature. To find out the feasibility of the materials as next-generation hydrogen storage materials, we have performed comprehensive first-principles computer simulations of structural stability, electronic behavior, optical response, elastic properties, and thermodynamic properties of the materials. By giving the first generalized theoretical comprehension of these compounds, this publication contributes to the overall advancement of the sustainable hydrogen-based energy technologies and assists in the identification of the possible candidates in the further application as clean energy sources.

This paper is structured as follows. An outline of the calculating techniques is provided in Section 2. The structural features that were achieved by maximizing the energy as a function of volume are presented and discussed in Section 3. The electronic, elastic, thermodynamic, and phonon properties of both substances are examined in the same section. The final portion brings the climax to a close.

2 Computational analysis

This paper explored some functional properties of manganese-based perovskite hydrides, $YXMnH_6$ (X = Hg, Zn). The WIEN2k [28, 29] was used in computational analysis, which is based on the framework of Density Functional Theory (DFT), and it uses the Full-Potential Linearized Augmented Plane Wave (FP-LAPW) method [30, 31] to compute the electronic, mechanical, and optical properties. The projector-augmented wave (PAW) formulation of Quantum Espresso (QE) was examined for its vibrational and thermodynamic properties [32]. Instead, because of the QE program's effective density-functional perturbation theory (DFPT) implementations, phonon dispersion relations and associated thermodynamic variables were also computed. Perdew, Burke, and Ernzerhof's (PBE) method [33] was proposed using the Generalized Gradient Approximation (GGA); structural, electronic, mechanical, and optical properties were evaluated using the change-correlation function. For electronic structure research, the Tran-Blaha modified Potential Bekke-Johnson (TB-mBJ) [34] has been used; this potential yield results that are closer to the experimental outcomes compared to traditional PBE-GGA functionals. The plane-wave parameter $R_{MT} \times K_{max} = 7$ was used to cut off with optimization to hydrogen-based systems. In this case, R_{MT} is the smallest muffin-tin radius, and K_{max} is the maximum value of the k-vector. The two parameters, G_{max} and l_{max}, were set at value expansion of angular momentum at 16 and 10, respectively. A dense mesh of 1,000 k-points is used for the Brillouin zone [35] integration. In structural optimization, the system's total energy was minimized with respect to atomic locations and unit cell volume until energy convergence was reached at a threshold below 10^{-4} Ry. Birch-Murnaghan's equation [36] was used for structural optimization in order to determine bulk moduli and equilibrium lattice parameters. To describe the electronic behavior of the valence and conduction bands, band structures and density of states (DOS) were examined. The WIEN2k's IRelast package [37] used the stress-strain method [38] to determine the mechanical elastic constants. The Voigt–Reuss–Hill (VRH) [39] averaging approach was utilized to test additional mechanical properties using the derived elastic constants. The Kramers-Kronig formulas were used to study optical parameters such absorption coefficients, refractive index, and reflection [40]. The dielectric function was done using the WIEN2k optics module, in which the optical matrix elements are determined on a 10,000-point dense mesh of k-points. Phonon dispersion [41] spectra calculated by DFPT as provided by QE to check dynamic stability of the studied material. Lastly, the system's thermodynamic stability was checked at T = 300 K by *ab initio* molecular dynamics (AIMD) simulations in the NVT ensemble in the presence of a Nosé–Hoover thermostat with a time step $\Delta t = 1$ fs and a total simulation duration of 5 ps (5,000 fs).

3 Results and discussion

3.1 Structural properties

In this section of studies, specific aspects of crystallographic features, including the structural parameters, and energy-to-volume correlations of $YXMnH_6$ hydrides, where X represents either Hg or Zn, are discussed. Which gives a general overview of their suitability as candidates for effective energy storage material. Figure 1 indicates that the modeled perovskite compounds $YHgMnH_6$ and $YZnMnH_6$ both have a face-centered cubic (FCC) structure, with space group F $\bar{4}$ 3 m (No. 216). In the given structural arrangement, the atoms in $YHgMnH_6$ and $YZnMnH_6$ occupy distinct fractional coordinate positions within the unit cell in order to enhance both the hydrogen storage capacity and the lattice stability. The atomic arrangements were generated using the WIEN2k software package. The locations of the yttrium (Y) sites at $(\frac{1}{2},0,0)$, manganese (Mn) located at $(\frac{1}{4},\frac{1}{4},\frac{1}{4})$, and X (Hg and Zn) atoms are located at (0, 0, 0). As the interstitial voids of the lattice are filled by the hydrogen atoms (H_2) $(\frac{1}{4},\frac{1}{4},x)$, forming an optimized geometric configuration that ensures high-efficiency hydrogen storage from both volumetric and gravimetric terms.

The structural characteristics of the compound were examined using the Birch-Murnaghan equation of state [42]. The total energy (E_t) was computed with different lattice parameter values in a range of volumes to determine which kind is the most stable configuration. The Birch-Murnaghan Equation of State (EOS) can be expressed mathematically as in Equation 1, where E(V) is the energy as a function of volume; E_0 is the equilibrium energy at the optimized equilibrium volume V_0; B is the bulk modulus; (B′) is the bulk modulus's pressure derivative with respect to pressure (P); and V is the actual volume at 0 K and 0 GPa.

$$E(V) = E_0 + \frac{9BV_0}{16}\left[\left(\left(\frac{V_0}{V}\right)^{\frac{2}{3}} - 1\right)^3 B' + \left(\left(\frac{V_0}{V}\right)^{\frac{2}{3}} - 1\right)^2 \left(6 - 4\left(\frac{V_0}{V}\right)^{\frac{2}{3}}\right)\right] \quad (1)$$

Pressure (P) and volume (V) can be connected to the bulk modulus through the following relationship $B = -V\frac{dP}{dV}$ in which pressure can be defined as in Equation 2 [43]:

$$P(V) = -\frac{dE}{dv} = \frac{b}{B'}\left[\left(\frac{V_0}{V}\right)^{B'} - 1\right] \quad (2)$$

The parabolic energy–volume (E–V) curves of the materials under discussion, which show the connection between the total energy and the volume of the unit cell of both compounds, are shown in Figures 2a,b. The investigated lattice parameters corresponding to the minimum energies E_0 were determined. $YHgMnH_6$ has the largest lattice constant (6.85 Å), which is higher compared to $YZnMnH_6$ (6.65 Å). The increase in the lattice lengths is due to the fact that the atomic radii of mercury are bigger in comparison to zinc atoms. The volume unit cell (V) increases with the increase of the ionic radius, with $YHgMnH_6$ having the largest one (544.13 $Å^3$) and $YZnMnH_6$ having the smallest (496.26 $Å^3$). We observed, as indicated in Table 1, the expected trends in the lattice constant parameters (a) and unit cell volumes (V) with increasing atomic size.

The differences of the bulk modulus (B) and its first-order pressure derivative (B′) give useful data on the behavior of the

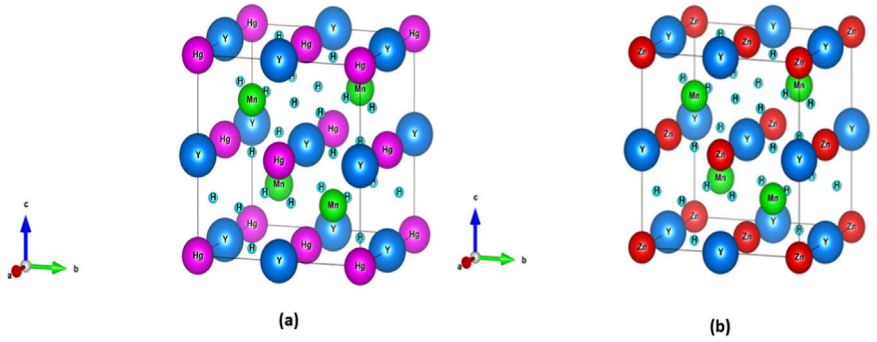

FIGURE 1
The crystal structure of **(a)** $YHgMnH_6$ **(b)** $YZnMnH_6$.

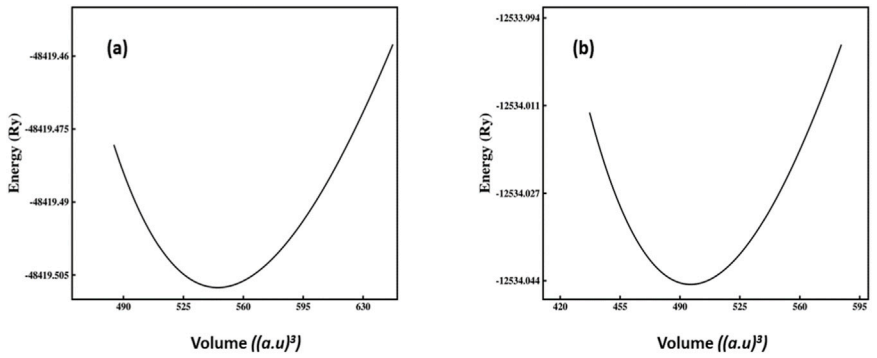

FIGURE 2
The optimized energy-volume graphs of $YXMnH_6$ (X = Hg, Zn). **(a)** $YHgMnH_6$, **(b)** $YZnMnH_6$.

TABLE 1 Lattice parameter (a, Å), volume (V, Å^3), bulk modulus (B, GPa), bulk modulus derivative (B′), total energy (E_0, Ry), and Bandgap (E_g, eV) using GGA and mBJ approximation of $YHgMnH_6$ and $YZnMnH_6$ hydrides.

Compound	a	V	B	B′	E_0	E_g (GGA)	E_g (mBJ)
$YHgMnH_6$	6.8623	545.19	102.77	4.0586	-48419.50	1. 445	1.826
$YZnMnH_6$	6.6506	496.26	110.45	3.7749	-12534.04	1.555	2.548

material to compress and its level of softness under pressure. It is seen that the calculated results indicate that the compound that contains Zn has a higher bulk modulus value (110.45 GPa), indicating greater stiffness and less compressibility compared to the Hg-based compound (102.63 GPa). Even though $YHgMnH_6$ is comparatively softer at room temperature, its B′ greater than $YZnMnH_6$ implies that it could become stiffer when put under external pressure. Furthermore, the ground-state energy (E_0) gives essential data on the thermodynamic behavior of compound stability, in which the lower E_0 values correspond to a more stable structure [44]. It could be noted by comparing the calculated values of energy at zero pressure and absolute zero temperature that $YHgMnH_6$ has lower E_0 values (−48419.50Ry), compared to the value of E_0 (−12534.04Ry) of $YZnMnH_6$, that because the absolute total energies (E_0) from all-electron calculations are related to the binding energies of the core electrons of the constituent atoms. The significantly lower total energy of $YHgMnH_6$ compared to $YZnMnH_6$ is physiochemically explained by the fact that the atomic number and the core energy of Hg (Z = 80) are larger than that of Zn (Z = 30). Table 1 shows the calculated equilibrium structural parameters of the two cubic structures. These compounds have not been studied previously, offering a basis of comparison with studies in the future.

3.2 Electronic properties

It is well recognized that one of the most basic procedures of materials science is comprehending a material's electronic structure, which characterizes the distribution and behavior of electrons inside its atomic or molecular framework. The electronic band structure

and densities of state (DOS) of the hydride compounds $YHgMnH_6$ and $YZnMnH_6$ were examined using the PBE-GGA and mBJ-GGA methods at the equilibrium lattice constant in order to study their electronic behavior. By using this approach, we can better understand the nature of chemical bonding and categorize the materials according to their behavior as conducting, insulating, or semiconducting [45].

The electronic band structures of $YHgMnH_6$ and $YZnMnH_6$ were calculated through the first Brillouin zone at 0 K as a function of wave vector K, within the energy range from −10 eV to +6 eV, listed in Figure 3. In this computation, the horizontal red dashed line indicates the Fermi level (E_F) as a reference energy at 0 eV. For ensuring the accuracy of results, we are choosing in this study both the PBE-GGA and enhanced by mBJ-GGA methods, which were employed to predict accurate electronic properties, providing a comparison between standard and enhanced approximations. The valence band (VB) and conduction band (CB) are represented by the negative and positive energy regions, respectively. The energy range separating the bottom of CB and top of VB, where no electronic states exist, is called the band gap (E_g) [46]. It is mathematically calculated by Equation 3:

$$E_g = E_{CBM} - E_{VBM} \tag{3}$$

It is evident that the conduction and valence bands do not overlap at the Fermi level, indicating that both hydride perovskites are semiconducting. Additionally, the conduction band minimum and valence band maximum occur at distinct symmetry positions, suggesting that both hydride perovskites are indirect band gap semiconductors. It is evident that the PBE-GGA and mBJ-GGA approaches provide different anticipated band gap values. Band gaps for $YHgMnH_6$ and $YZnMnH_6$ are predicted by the PBE-GGA calculation to be 1.445 eV and 1.555 eV, respectively. However, the application of the mBJ-GGA dramatically increases the, E.g., values for both hydrides under study, indicating much wider band gap values of 1.826 eV for $YHgMnH_6$ and 2.548 eV for $YZnMnH_6$, respectively. This improvement highlights the accuracy and reliability of the mBJ functional that addresses the well-known bandgap underestimation issue of the standard PBE-GGA, consistent with the benchmarking of the mBJ potential in perovskite-type systems.

The total density of states (TDOS) and projected density of states (PDOS) are important studies towards the understanding of electronic properties in materials. These calculations give more detail about the orbital (s, p, and d) contributions and electronic structure at the Fermi level. The electronic density of state is the unit of energy band that electrons can occupy in a unit of electron states [47]. Figure 4 shows the TDOS and PDOS of $YHgMnH_6$ and $YZnMnH_6$ calculated in PBE-GGA and GGA-mBJ approximations. Figure 4 indicates that the TDOS confirms the existence of a distinct band gap at the Fermi level, as per the findings of the electronic band structure of the studied hydride materials. The vertical black dashed line shows the E_F set at 0 eV and taken as a reference. We analyzed PDOS to gain additional insight into the atomic and orbital contributions that can find out the electrical nature of the compounds.

The PDOS for $YHgMnH_6$ is shown in Figures 4(a,b) in the energy range of −10 to 6 eV. The Hg-d states, which have the largest contribution between −8 and −6 eV, are represented by a prominent peak in the valence band (VB) region. Mn-d states predominate in the valence band between −2 eV and 0 eV, while H-s and Y-d states contribute very little to VB. It also demonstrates that Mn-d and Y-d orbitals contribute significantly to the CB energy range of 0–6 eV. The H-s and Hg-s contributions are minimal in this CB region. There are also several contributions in the valence band region of $YZnMnH_6$ (−10 eV–0 eV) (Figures 4(c,d)). (Y, Mn, and Zn-d) and H-s orbitals make significant contributions near the Fermi level; these orbitals are quite dominant in the valence band, highlighting the important hydrogen-metal interactions and their role in bonding interactions [48]. However, the contributions from the Y-s, Y-p, Zn-s, Zn-p, Mn-s, and Mn-p orbitals are minimal. The Mn-d and Y-d states become increasingly delocalized and contribute the most in the conduction band (CB) (0 eV–6 eV), with small contributions from the Zn-s and H-s states.

The broader band gap observed in $YZnMnH_6$ (2.548 eV) compared to $YHgMnH_6$ compounds is because of the stronger hybridization between Zn-d and H-s orbitals. This is because this hybridization seems to push the minimum CB to higher energies. In contrast, a reduction of the band gap is due to the heavier Hg atom. Notably, the hybridization between H-s and metal p/d states refers to a strong H-M bonding, which is a decisive factor in storing hydrogen. These interactions indicate that although strong hybridization is possible for stabilized storage of hydrogen by hybridization, the presence of antibonding states near the minimum CB may facilitate the release of hydrogen under the external excitation [25]. Flat bands are those with a low dispersion, meaning that the energy is nearly constant with respect to the wave vector (k). Mathematically, the group velocity of electrons is given by $v_g = \frac{1}{\hbar}\frac{dE}{dK}$ so that the presence of a flat band $\left(\frac{dE}{dK} \approx 0\right)$ means that the group velocity is very small. So, the electrons in these states are strongly bound to their original atomic sites and have little itinerant behavior across the crystal lattice.

3.3 Optical properties

The study of optical characteristics of the $YXMnH_6$ (X = Hg, Zn) hydride material plays a vital role in determining its potential applications suitability in optoelectronic devices, as it reveals how the material interacts with light through absorption, reflection, and transmission [25]. The materials investigated in this study are semiconductors, as confirmed by their electronic properties. The optical behavior of such materials is primarily influenced by inter-band electronic transitions, which provide a deep understanding of the emission and absorption of light in optoelectronic systems [49].

In order to describe the interaction between light and matter depicted in Figures 5–7, the optical properties investigated for both $YHgMnH_6$ and $YZnMnH_6$ are calculated using PBE-GGA. These properties include the fundamental characteristics (real and imaginary) of the dielectric function $\varepsilon(\omega)$, absorption coefficients α (ω) refractive index n (ω), and reflection R (ω), respectively, all of which are related to frequency and energy. Optical properties vary with frequency, so the complicated dielectric function $\varepsilon(\omega)$ expressed by Equation 4 is used to explain these interactions, consisting of two components: the real part $\varepsilon_1(\omega)$, which defines the material's capacity to store electrical energy, reflecting its polarization response to an applied electromagnetic field, and the

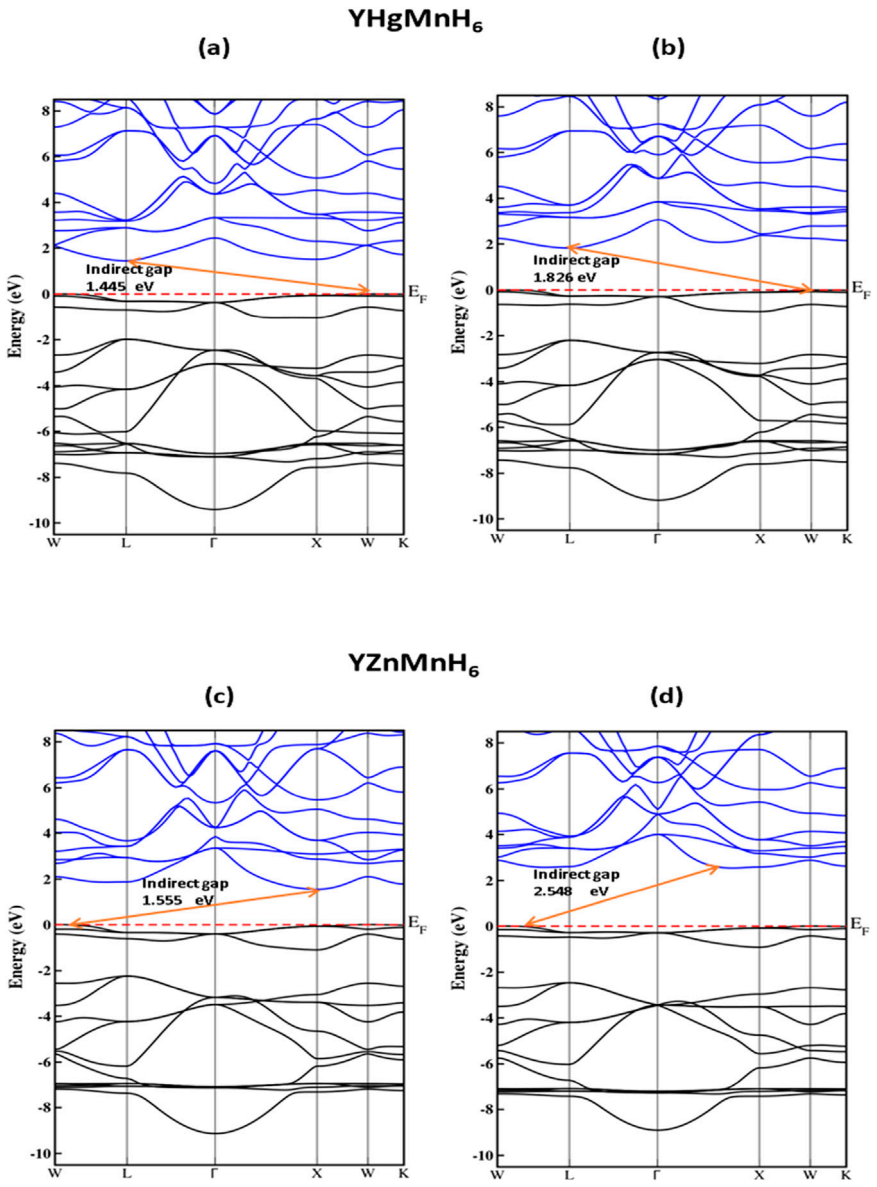

FIGURE 3
Electronic band diagrams of $YXMnH_6$ (X = Hg and Zn) perovskite hydrides calculated using PBE-GGA **(a,c)**, and mBJ-GGA **(b,d)** at ambient conditions.

energy dissipation as heat represented by the imaginary part $\varepsilon_2(\omega)$, which shows how the material absorbs and loses electromagnetic energy. The mathematical relation in the $\varepsilon_1(\omega)$ and $\varepsilon_2(\omega)$ parts of the dielectric function can be analyzed using the fundamental tool Kramers–Kronig relation described by Equations 5 and 6 [50].

$$\varepsilon(\omega) = \varepsilon_1(\omega) + i\varepsilon_2(\omega) \tag{4}$$

Where the real and imaginary components expressed as:

$$\varepsilon_1(\omega) = 1 + \frac{2}{\pi} P \int_0^{\infty} \frac{\omega' \varepsilon_2(\omega')}{\omega'^2 - \omega^2} d\omega \tag{5}$$

$$\varepsilon_2(\omega) = \frac{4\pi^2 e^2}{\pi \omega^2 m^2} \sum_{ij} \int_{BZ}^{\infty} \left[M_{ij}(K)\right]^2 f_i\left(1 - f_j\right) \delta\left[E_f - E_i - \omega\right] d^3k \tag{6}$$

In the above equations, P is the Cauchy integral, e^2 is the squared electronic charge and $M_{ij}(k)$ denotes the dipole matrix.

Since all other optical parameters are interconnected through the dielectric function, analyzing $\varepsilon_1(\omega)$ and $\varepsilon_2(\omega)$, it is important to provide insights into its suitability for optoelectronic and photonic applications. Which can be calculated using Equations 7–10 [51]

$$n(\omega) = \left[\frac{\sqrt{\varepsilon_1^2(\omega) + \varepsilon_2^2(\omega)} + \varepsilon_1(\omega)}{2} \right]^{\frac{1}{2}} \tag{7}$$

$$k(\omega) = \left[\frac{\sqrt{\varepsilon_1^2(\omega) + \varepsilon_2^2(\omega)} - \varepsilon_1(\omega)}{2} \right]^{\frac{1}{2}} \tag{8}$$

$$\alpha(\omega) = \sqrt{2\omega} \left[\sqrt{\varepsilon_1^2(\omega) + \varepsilon_2^2(\omega)} - \varepsilon_1(\omega) \right]^{\frac{1}{2}} \tag{9}$$

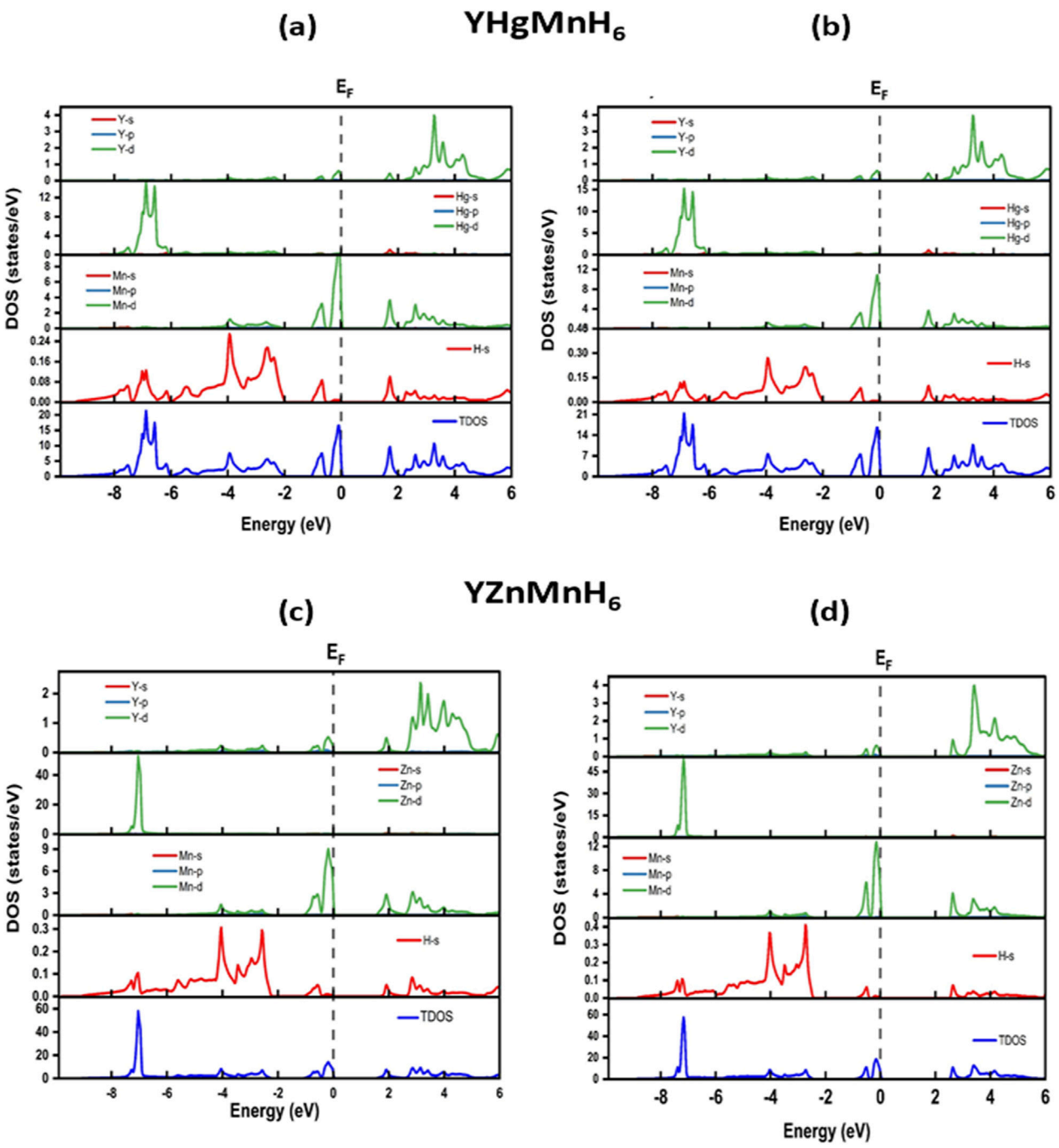

FIGURE 4
TDOS and PDOS of $YXMnH_6$ (X = Hg, Zn) were computed using the PBE–GGA **(a,c)** and mBJ-GGA **(b,d)** approximation. The vertical black dashed line represents the Fermi level (E_F).

$$R(\omega) = \left| \frac{\sqrt{\varepsilon_1(\omega) + i\varepsilon_2(\omega)} - 1}{\sqrt{\varepsilon_1(\omega) + i\varepsilon_2(\omega)} + 1} \right|^2 \tag{10}$$

The calculated real and imaginary parts of the dielectric function are displayed in Figures 5a,b within the energy range 0–13 eV, and this covers infrared (IR), visible, and ultraviolet (UV) energy ranges, respectively. The static values of the real part $\varepsilon_1(0)$ for $YHgMnH_6$ and $YZnMnH_6$ are 7.90 and 6.80, respectively. These findings show the existence of high dielectric screening and thus indicate the possibility of high refractive index behavior in these materials. And then $\varepsilon_1(\omega)$ curves gradually increase with a lower photon energy range, with the largest peaks at 18.71 at 3.11 eV for $YHgMnH_6$ and 12.57 at 3.46 eV for $YZnMnH_6$, with positive $\varepsilon_1(\omega)$ values indicating normal dielectric behavior. A negative zone

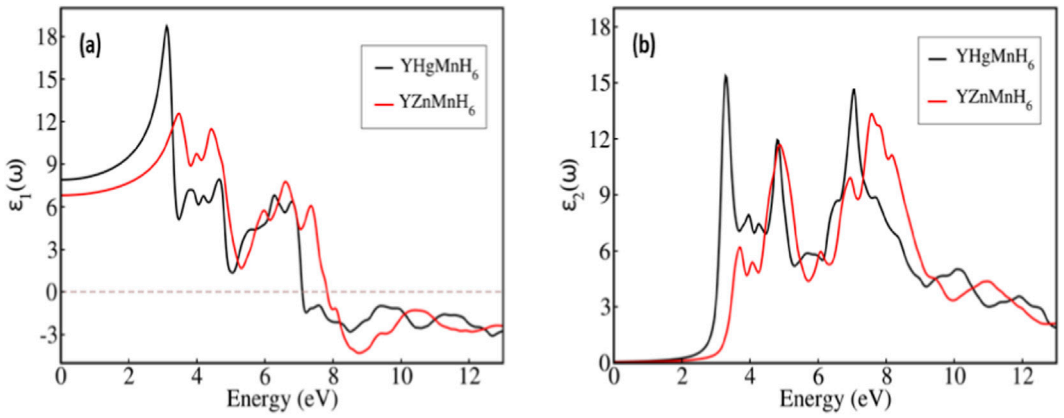

FIGURE 5
Dielectric function of $YHgMnH_6$ and $YZnMnH_6$ compounds **(a)** real part $\varepsilon_1(\omega)$, and **(b)** imaginary part $\varepsilon_2(\omega)$, by PBE-GGA approach.

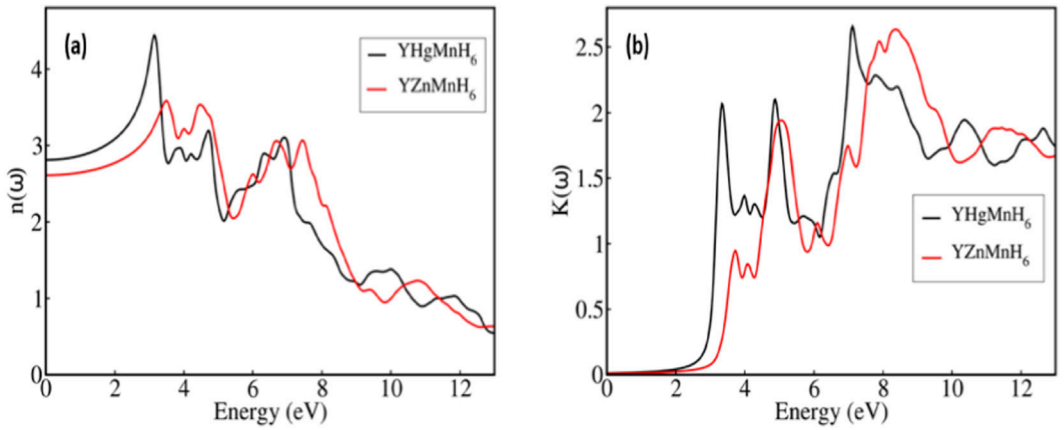

FIGURE 6
Optical refractive index of $YXMnH_6$ (X = Hg, and Zn) (a) Real part n(ω) and imaginary part K(ω).

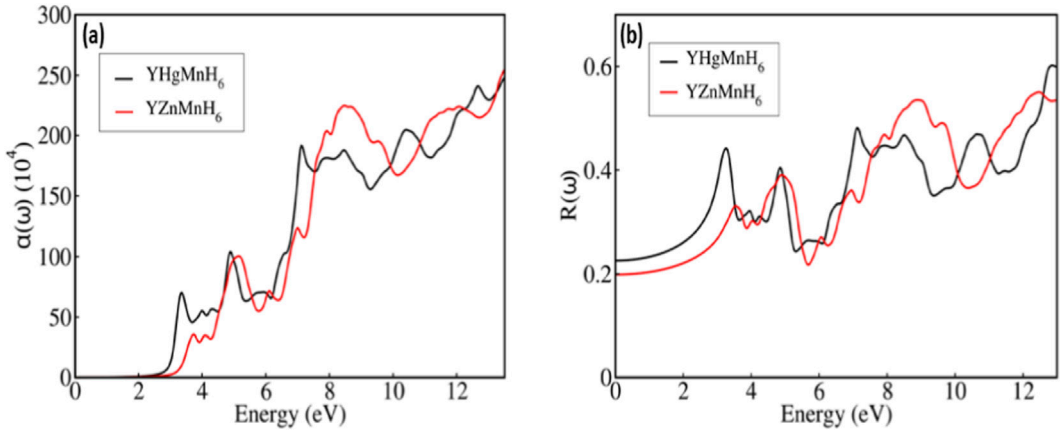

FIGURE 7
Optical parameters of $YXMnH_6$ (X = Hg, and Zn) **(a)** Absorption coefficient α(ω), and **(b)** Reflectivity R(ω).

TABLE 2 Calculated static optical parameters of $YHgMnH_6$, $YZnMnH_6$.

$n(0)$	R (0)	$\varepsilon_1(0)$	Compound
2.81	0.22	7.900	$YHgMnH_6$
2.60	0.19	6.809	$YZnMnH_6$

denotes plasma-like features observed at higher photon energies (7.11 eV for $YHgMnH_6$ and 7.85 eV for $YZnMnH_6$), indicating that the incoming electromagnetic frequency is greater than the effective plasma frequency. This shows the change from metallic to dielectric characteristics, where the material shows increased absorption and reflection of light. The investigated $\varepsilon_2(\omega)$ spectra displayed in Figure 5b with peaks appearing in the 3–8 eV range represent photon absorption caused by electronic transitions of d-states and H-s states. The primary peak values are 15.35 for $YHgMnH_6$ at 3.27 eV and 13.38 for $YZnMnH_6$ at 7.57 eV. Beyond 8 eV, $\varepsilon_2(\omega)$ gradually declines, which is consistent with the expected optical response of semiconducting materials.

Determining the real part n(ω) and complex part K(ω) of the refractive index $\tilde{n}$, as expressed in Equation 11, helps for understanding the optical behavior of a material. It is possible to assess the absorptive and dispersive properties of selected materials, which are obligatory to the formation of a large variety of optical equipment [52].

$$\tilde{n} = n + iK \tag{11}$$

The real refractive index n(ω) represents the extent to which the velocity of electromagnetic waves is decreased as it travels through a substance in contrast to a vacuum [53], and therefore n(ω) is necessary to consider in the design of optical devices, such as filters. Figure 6a shows n(ω) characterized against photon energy in the range 0–13 eV. The calculated static refractive index $n(0)$ values are consistent with the real part of the dielectric function $\varepsilon_1(\omega)$ through the relation equation $n(0) = \sqrt{\varepsilon_1(0)}$, is compatible with the static values of n(ω), calculated as 2.81 for $YHgMnH_6$, and 2.60 for $YZnMnH_6$, as listed in Table 2. Notable peaks appear within the 2–5 eV range, the found peak values of n(ω) are 4.44 at 3.14 eV and 3.58 at 3.49 eV for $YHgMnH_6$ and $YZnMnH_6$, respectively, which may indicate strong light-bending properties corresponding to the dispersion effects observed in $\varepsilon_1(\omega)$. As photon energy increases beyond 8 eV, the n(ω) curves gradually decline across both compounds. $YHgMnH_6$ has the greatest refractive index value, which indicates the compound's stronger polarization and more intense interaction with incident photons falling on its surface compared to that in $YZnMnH_6$. As a result, $YHgMnH_6$ is a well-known and emerging alternative for hydrogen storage and associated devices. While the imaginary part K(ω) is known as the capacity of the compound to absorb or scatter the incident light photons on its surface, causing loss of light intensity [54]. Peaks in K(ω) varied between 3 and 10 eV, as shown in Figure 6b, generally following the trends observed in $\varepsilon_2(\omega)$. As the photon energy exceeds 10 eV, the K(ω) values progressively decrease, suggesting lower optical attenuation in this region.

The absorption coefficient α(ω) is also another important quantity that defines the distance an incident light can travel in the material before being absorbed and defines the effectiveness of the material in absorbing the incident light in a particular energy range. If the absorption is high, the electrons in the material can easily be excited from occupied and unoccupied states [55]. This is related to the material's dielectric functions. The calculated α(ω) spectrum using PBE-GGA is shown in Figure 7a for the two perovskite hydrides, $YHgMnH_6$, and $YZnMnH_6$. The absorption coefficient α(ω) initially begins from zero in the absence of incident photon energy and then rises as the photon energy passes the optical energy gap of both compounds. The maximum absorption peak in the 3–9 eV range is for $YZnMnH_6$, appearing at 8.47 eV (224.97×10^4 cm^{-1}). While the maximal α(ω) peak of $YHgMnH_6$ is found to be 191.58×10^4 cm^{-1} at 7.11eV, another sharp peak is found at high UV range (12.66 eV) with a rate of 241.18×10^4 cm^{-1}. The highest absorption values can be used for hydrogen storage; these peaks indicate the material's ability to absorb photons; thus, they are promising candidates for photonic devices and UV photodetectors.

The reflectivity function R(ω) is used to determine the efficiency of a material to reflect incident light from the surface [56]. In Figure 7b, we present the reflectivity R(ω) of perovskite hydrides $YXMnH_6$ as a function of the incident photon energy (0–13 eV). The static reflectivity R(0) of $YHgMnH_6$ and $YZnMnH_6$ hydrides (see Table 2) are 0.22 and 0.19, respectively. At low energy range (<3 eV), $YHgMnH_6$ is more reflective, so more low-energy photons are reflected. At the 3–9 eV energy range, there are several oscillations, but $YZnMnH_6$ shows a higher peak at 9 eV, which means that there are more inter-band electronic transitions in this energy range than in $YHgMnH_6$. At higher energy ranges (9–13 eV), the reflectivity peaks increase, but $YHgMnH_6$ is higher at 12–13 eV, while $YZnMnH_6$ is lower. This suggests that complex electron rearrangements and interactions on the surface influence the interactions with electromagnetic waves in the broad energy range [57]. Overall, the maximum reflectivity peaks indicate that $YHgMnH_6$ is more likely to be reflected at low and high energy ranges, whereas $YZnMnH_6$ is reflected in the UV range.

Together, these obtained properties provide a complete picture of the optical response of $YXMnH_6$ material, allowing researchers to understand and predict its interaction with light, which is crucial in designing materials for optoelectronic applications, and exhibits the strongest optical responses for UV applications.

3.4 Mechanical properties

Mechanical properties of a material refer to the response of the material to the applied forces and can be investigated by the use of elastic constants (C_{ij}) [58]. As such, the elastic constants of cubic $YXMnH_6$ (X = Hg and Zn) compounds are evaluated in this study to determine how the material withstands shock, the elasticity of it, and its deformation response under applied stress. In addition, mechanical properties are necessary to assess their suitability for optoelectronic and energy storage applications. Cubic crystal is normally known to have only three elastic constants: C_{11}, C_{12}, and C_{44}. These constants describe the material's deformation response to uniaxial compression (C_{11}), whereas the positive values (C_{12}) reveal expansion transversely with the stress exerted, and (C_{44}) reflects the shear deformation resistance and material's hardness [59]. The estimated values of the elastic constancy of $YHgMnH_6$ and $YZnMnH_6$ are carefully described in Table 3, which may be

TABLE 3 Elastic constant (C_{ij}, GPa) of $YXMnH_6$ (X = Hg, Zn).

C_{44} (GPa)	C_{12} (GPa)	C_{11} (GPa)	Hydrides
56.58	35.68	262.14	$YZnMnH_6$
43.93	42.61	224.52	$YHgMnH_6$

employed to ascertain their stability by confirming the Born stability criterion [60]. The following are the conditions that the elastic constants should follow: $C_{11} > 0$; $C_{44} > 0$; C_{11}- $C_{12} > 0$; $C_{11} + 2C_{12} > 0$; $C_{12} < B < C_{11}$. The calculated elastic constants for each $YHgMnH_6$ and $YZnMnH_6$ are positive, which satisfies Born–Huang stability conditions and confirms the mechanical stability for the studied hydrides. As noted, $YZnMnH_6$ has a greater resistance to an axial compression with C_{11} = 262.14 GPa, compared to 224.52 GPa for $YHgMnH_6$. Secondly, the volumetric stiffness C_{12} is 42.61 GPa for $YHgMnH_6$, higher than 35.68 GPa for $YZnMnH_6$. Moreover, C_{44} values suggest that $YZnMnH_6$ (56.58 GPa) is harder compared to $YHgMnH_6$ (43.93 GPa).

Learning properties in elasticity. Such as bulk modulus, shear modulus, Young modulus, and Poisson's ratio, are used to identify the brittleness or ductile nature of a material. These properties are necessary and help in determining the right compound to be used in a particular application. For example, high-stiffness materials (a large Young's modulus) would be better in use in civil engineering applications. Different mechanical parameters can be calculated using the fundamental elastic constants, C_{11}, C_{12}, and C_{44}. These parameters were calculated using Voigt, Reuss, and Hill averaging methodologies [61, 62]. The Hill approximation was selected for the computations because it provides a more precise and practically accurate average of the Voigt and Reuss constraints, and it aligned very well with the experimental results [63]. This is because average (Hill) more accurately depicts the material's total reaction to mechanical stress by accounting for both the lower (Reuss) and higher (Voigt) limitations for the elastic modulus. The subsequent Equations 12, 13 employed elastic constants to calculate these mechanical moduli as follows:

$$B_V = B_R = \frac{1}{3}(C_{11} + 2C_{12}) \tag{12}$$

$$B = B_H = \frac{1}{2}(B_V + B_R) \tag{13}$$

In the above equation, B_H represents the Hill average of the bulk modulus, while B_V and B_R are the Voigt and Reuss averages of the bulk modulus, respectively. The bulk modulus (B) is a very important mechanical property that measures a material's resistance to volume compression under pressure [64]. This gives information about the material's stiffness and stability by measuring the material's resistance to volume changes under pressure. We calculated values for $YZnMnH_6$ (111.17 GPa), and $YHgMnH_6$ (103.25 GPa) that are much higher than those of the conventional magnesium hydride (MgH_2 approx. 51.0459 GPa [65]). This shows that the cubic perovskites investigated here have a greater structural stability under the high pressures required for hydrogen loading processes because they are less affected by volume changes.

$$G_V = \frac{1}{5}(C_{11} - C_{12} + 3C_{44}) \tag{14}$$

$$G_R = \frac{5C_{44}(C_{11} - C_{12})}{[4C_{44} + 3(C_{11} - C_{12})]} \tag{15}$$

$$G = G_H = \frac{1}{2}(G_V + G_R) \tag{16}$$

$$E = \frac{9\,BG}{3B + G} \tag{17}$$

$$\nu = \frac{(3B - 2G)}{2(3B + G)} \tag{18}$$

Here in Equations 14–18, G_V, G_R, G_H, E, and ν stand for Voigt shear modulus, Reuss shear modulus, Hill shear modulus, Young's modulus, and Poisson's ratio, respectively. Shear modulus (G) is defined to describe the resistance to shear deformation and provides a measure of the material's resistance to the change of shape, which is reversible under the effect of shear stress [66]. The high G value found for $YZnMnH_6$ (74.99 GPa), and a low G value for $YHgMnH_6$ (59.06 GPa) indicated high and low resistance to shear, respectively. Young's modulus (E) is the ratio of stress to the strain, which measures the stiffness of the material. In Table 4, $YZnMnH_6$ exhibits the highest E-value, 183.68 GPa, which shows the stiffness of the material with respect to 148.81 GPa for $YHgMnH_6$.

To gain a better insight into the mechanical stability of these hydrides, the brittle or ductile nature of a material can be evaluated by means of the Poisson ratio (ν), the Pugh ratio (B/G), and the Cauchy pressure (Cp). (B/G) can be written as the ratio of the bulk modulus to the shear modulus. Pugh's ratio has a critical value of 1.75, which is often used to distinguish between brittle and ductile materials. If the Pugh ratio is less than 1.75, then the material is brittle in nature; if it is more than 1.75, it is ductile in nature [67]. The bonding nature can be explained by Cauchy pressure (Cp), which can be calculated from $C_p = C_{12} - C_{44}$. Brittleness and covalent bonding are indicated by a negative C_p value, while ductile behavior and an ionic bonding character are indicated by a positive C_p value [68]. In a similar way, the Poisson ratio (ν) is also another parameter used to distinguish between ductile and brittle materials; it describes the material's behavior in the direction perpendicular to an applied force. According to the (B/G) ratio, $YHgMnH_6$ (1.74) and $YZnMnH_6$ (1.48) are less than 1.75. Negative values of C_p are −20.90 GPa and −1.32 GPa for $YZnMnH_6$ and $YHgMnH_6$, respectively. Also, ν values (0.26 and 0.22) as listed in Table 4. According to this value, $YZnMnH_6$ indicates a brittle structure, and $YHgMnH_6$ exhibited brittle behavior but close to the brittle-ductile threshold.

The Zener anisotropy factor (A) measures the degree of direction in the response to elasticity. According to Equation 19, when A equals 1, a material becomes isotropic meaning that its mechanical properties are the same in every direction. However, a divergence from one indicates that the material is anisotropic, or in other words, its mechanical characteristics differ in various directions [69, 70]. $YZnMnH_6$ and $YHgMnH_6$ have an A value of 0.60 and 0.66, respectively. These results suggest that $YXMnH_6$ (X = Hg, Zn) possesses high elastic anisotropy. In short, the mechanical test verifies that $YZnMnH_6$ is anisotropic, brittle, stiff, and has high deformation resistance. $YHgMnH_6$ has B/G ratios that are advantageous for applications needing flexibility and directional adaptation, as well as Cp values that are almost neutral and higher

TABLE 4 Calculated mechanical characteristics of $YXMnH_6$ (X = Hg, Zn).

Cp (GPa)	B/G	ν	A	E (GPa)	G (GPa)	B (GPa)	Materials
−20.90	1.48	0.22	0.60	183.68	74.99	111.17	$YZnMnH_6$
−1.32	1.748	0.26	0.66	148.81	59.06	103.25	$YHgMnH_6$

(v = 0.26).

$$A = \frac{2C_{44}}{C_{11} - C_{12}} \tag{19}$$

3.5 Thermodynamic properties

The thermodynamic properties of the investigated Y-based hydride perovskites $YZnMnH_6$, and $YHgMnH_6$ hydrides were examined through the quasi-harmonic Debye model to determine their thermal and temperature-sensitive behavior. It allows one to assess their usability as the hydrogen storage medium. The goal of the current study was to compute the fundamental thermodynamic quantities of the $YZnMnH_6$ and $YHgMnH_6$ in the form of entropy (S), internal energy (E), heat capacity with constant volume (C_v), and Helmholtz free energy (F), on a large-scale basis of temperature between 0 and 800 K, as described in Equations 20–23. This kind of analysis will be useful in understanding the thermodynamic response of the compounds in different thermal conditions [60].

$$S(T) = k_B\left\{\int \frac{\hbar\omega/k_BT}{\exp(\hbar\omega/k_BT)-1}F(\omega)d\omega - \int F(\omega)\ln\left[1-\exp(-\hbar\omega/k_BT)\right]d\omega\right\} \tag{20}$$

$$C_V(T) = k_B\int \frac{(\hbar\omega/k_BT)^2\exp(\hbar\omega/k_BT)}{[\exp(\hbar\omega/k_BT)-1]^2}F(\omega)d\omega \tag{21}$$

$$E(T) = E_{tot} + E_{zp} + \int \frac{\hbar\omega}{\exp(\hbar\omega/k_BT)}F(\omega)d\omega \tag{22}$$

$$F(T) = E_{tot} + E_{zp} + k_BT\int F(\omega)\ln\left[1-\exp(-\hbar\omega/k_BT)\right]d\omega \tag{23}$$

Where E_{zp} is the zero-point vibrational energy in term of F(ω) which is the phonon density of states, defined as in Equation 24:

$$E_{zp} = \frac{1}{2}\int F(\omega)\hbar\omega d\omega \tag{24}$$

A basic thermodynamic quantity that characterizes a material system's disorder is entropy (S). With increasing temperature, the thermal vibration of atoms and the lattice vibration increase, causing the level of disorder and the thermal energy stored in the system to increase [71]. The calculated results in Figures 8a, c demonstrate a typical thermodynamic trend of the growing values of entropy and energy with temperature for both compounds; it implies a higher level of structural and vibrational disorder, thermodynamically most favorable dehydrogenation, and also enables hydrogen desorption at high temperatures to take place. Among the current compounds, $YZnMnH_6$ has the smallest entropy change, which means that it is the most ordered and has more degrees of freedom to store hydrogen and thus is more suitable for storing hydrogen. However, has the largest entropy variation, which means that it has the largest vibration disorder and, therefore, is the most likely to desorb hydrogen, particularly at higher temperatures [60].

In Figure 8b, the heat capacity (C_V) dependence on temperature reveals important details about the lattice vibrational behavior. It is seen at low temperatures (0–600 K) to depend strongly on temperature and follow the expected T^3 dependence of the Debye theory, and this reveals that low-frequency (acoustic) phonon modes are responsible for the heat capacity in this temperature regime. This is also typical of well-crystalline solids, for which the thermal excitations are dominated by low-frequency lattice vibrations. At higher temperatures (T > 600 K), the rate of increase of CV decreases and saturates at higher temperatures towards the expected Dulong-Petit limit ($C_V \rightarrow 3R$) as is common to well-behaved crystalline materials [72]. The Helmholtz free energy (F) shows a decreasing trend with temperature, which implies that the structures are stable at higher temperatures. This behavior is required for high-temperature applications, such as, hydrogen release, and demonstrates the stability of the hydrides at high temperatures. Free energy diagrams (Figure 8d) show that $YHgMnH_6$ is more stable than $YZnMnH_6$ as the effect of atomic vibrations increases since it has lower free energy at elevated temperatures. These findings demonstrate the thermodynamic stability of $YXMnH_6$ (X = Hg, Zn) hydrides in the temperature range studied and give insight into hydrogen storage and release.

3.6 Lattice dynamic stability

The phonon dispersion curve of perovskite hydrides $YXMnH_6$ (X = Hg, Zn) was performed along (Γ, X, U, L, W) symmetry points of the Brillouin zone to understand how stable these materials are when atoms vibrate [73]. To investigate the dynamic and structural stability at absolute zero temperature, phonon dispersion calculations were done and are presented in Figure 9, where 27 phonon modes, including 24 optical modes, and three acoustic modes, are displayed. The phonon spectra of the two $YZnMnH_6$ and $YHgMnH_6$ obtained do not have any imaginary frequencies (i.e., no frequencies below zero), which are found mostly in the lower acoustic branches, indicating that the two investigated materials are dynamically stable. The phonon dispersion curve revealed that the vibrational modes of H-atoms make up the high-frequency portion. The $YZnMnH_6$ compound has the highest phonon frequency around 31 THz is particularly significant since it indicates that H-metal bonds are stronger than those in $YHgMnH_6$ compounds. This resolute connection can result to enhanced bond stiffness on hydrogen in the lattice crystal. In the case of the $YHgMnH_6$ compound, the maximum frequency is approximately 27 THz, and the bonds between H and metal were weaker. It is advantage of the high-temperature stability. In addition, the Hg weighs considerably more than Zn, and as a result, the compound containing Hg is

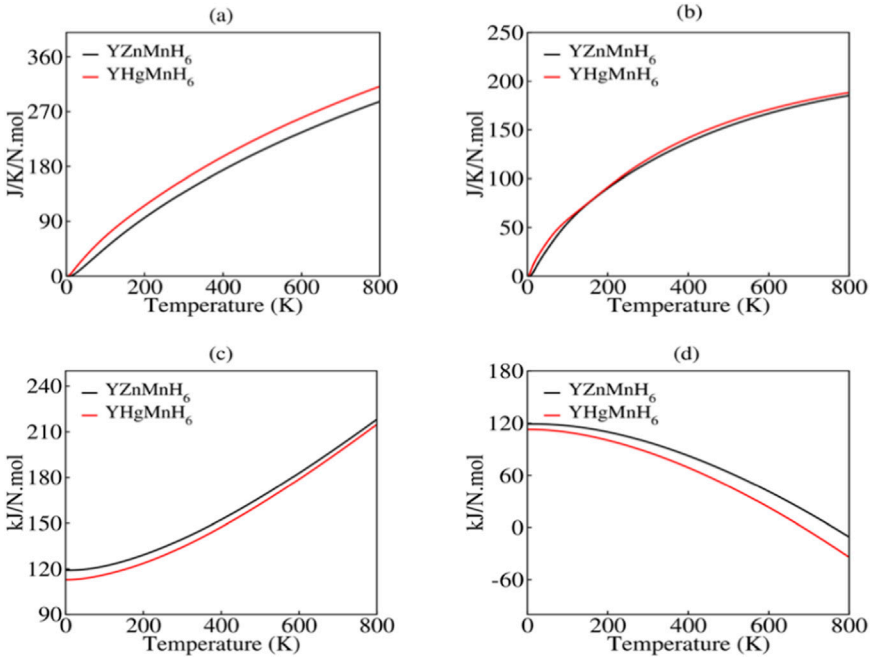

FIGURE 8
The change in entropy, internal energy, heat capacity, and free energy with the temperature of $YXMnH_6$ (X = Hg, Zn) hydrides. **(a)** Entropy (S) **(b)** Heat Capacity C_V **(c)** Energy (E) **(d)** Free Energy (F).

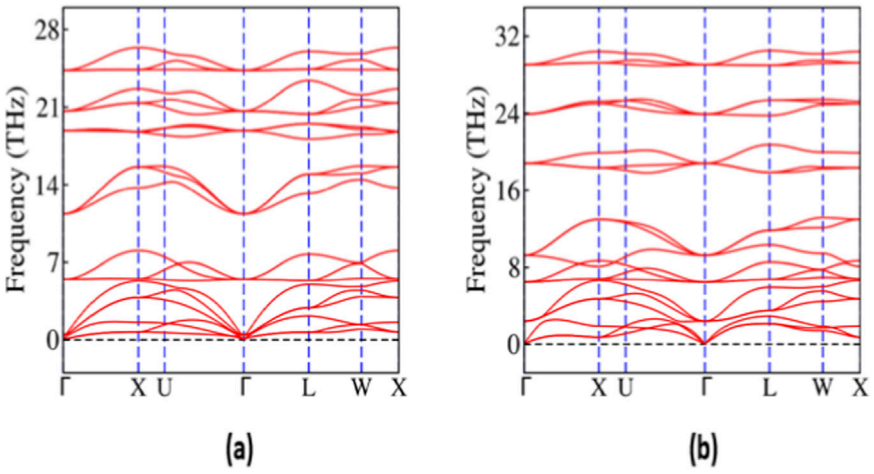

FIGURE 9
Phonon dispersion curves of $YXMnH_6$ (X = Hg, Zn) compound. **(a)** $YHgMnH_6$ **(b)** $YZnMnH_6$.

likely to show a few smaller phonon frequencies in the acoustic and low-optical spectrum than one in which it is replaced by Zn. This mass-dependent vibrational property is very essential in deciding the dynamical stability as well as the characteristics of hydrogen bonding of these materials.

The continuous transition between the acoustic and low-frequency optical branches suggests a moderate coupling of acoustic–optical phonons, allowing the transfer of vibrational energy all over the lattice. Moreover, the high-frequency optical modes are mainly associated with hydrogen vibrations. These are dispersive, indicating finite coupling between hydrogen and the host lattice, and the absence of soft hydrogen-related modes confirms the dynamical stability of the hydrogen atoms, which could have a positive effect on the thermally activated hydrogen mobility in the host lattice.

3.7 Molecular dynamics analysis

Ab initio molecular dynamics (AIMD) simulations were used to study the simulation of the dynamical behavior and thermal

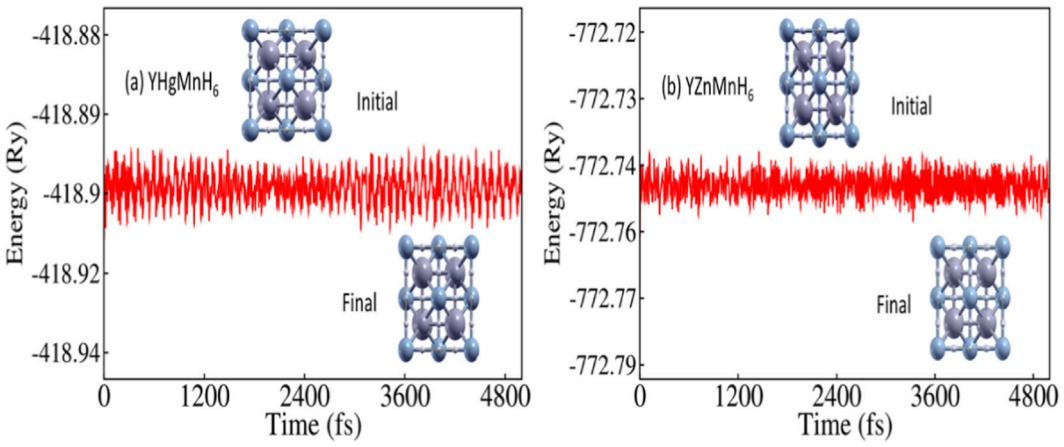

FIGURE 10
Total energy fluctuation of perovskite compounds $YXMnH_6$ (X = Hg, Zn) as a function of time estimated in AIMD simulations at 300K: **(a)** $YHgMnH_6$ **(b)** $YZnMnH_6$.

stability of the perovskite hydrides $YXMnH_6$ (X = Hg, Zn). To this end, $YZnMnH_6$ and $YHgMnH_6$ were simulated during a period of time of 5 ps at room temperature in order to investigate the changes in the total energy as a function of time [25], as shown in Figure 10. The overall dynamics of energy variations in $YXMnH_6$ compounds under study remain steady and consistent over the entire period of simulation. For $YZnMnH_6$, the equilibrium energies are limited to a range of −772.76 Ry to −772.73 Ry, whereas for $YHgMnH_6$, they fall between −418.91 Ry and −418.89 Ry. The absence of thermal instability or structural collapse under limited temperature settings is suggested by these modest scale energy vibrations. This behavior is in line with the previous studies of comparable hydride systems, such as $NaScFeH_6$ and $KBaGaH_6$ [19, 48]. The small variations in energy fluctuations establish that both hydrides of $YXMnH_6$ maintain their structural and dynamical stability at room temperature. This is one of the major requirements of the materials to be used in the hydrogen storage application since it guarantees them against thermal perturbation levels and helps in making them viable regarding the reversible and sustainable hydrogen absorption and desorption mechanisms [74]. Importantly, the host framework is maintained during the simulation trajectory, which confirms that the perovskite hydrides structure is reversible. It means that materials are able to survive the thermodynamic conditions of hydrogen cycling without irreversible decomposition into binary phases, proving their appropriateness for cyclic hydrogen storage applications.

3.8 Thermal stability and hydrogen storage properties

As a crucial metric for evaluating thermodynamic stability of $YXMnH_6$ (X = Hg, and Zn), the formation enthalpy. Therefore, ΔH of $YXMnH_6$ hydrides are defined as follows Equations 25, 26 [69, 75]:

$$\Delta H = \sum E_{\text{products}} - \sum E_{\text{reactants}} \tag{25}$$

$$\Delta H = \frac{E_{total}^{\text{YXMnH}_6} - \left(E_{tot}^{Y} + E_{tot}^{X} + E_{tot}^{Mn} + 3E_{tot}^{H_2}\right)}{N} \tag{26}$$

In the provided equation, E_{products}, $E_{\text{reactants}}$ are the total energies of the products and reactants, respectively. $E_{total}^{\text{YXMnH}_6}$ donates the total energy of optimized compounds, whereas, $E_{tot}^{Y}, E_{tot}^{X}, E_{tot}^{Mn}, and\, E_{tot}^{H_2}$ refers to the ground state energies of one Y, X, Mn atoms and the H_2 molecules, respectively. The negative value of ΔH means that the studied materials form an exothermic formation reaction. This implies that the hydride itself is energetically more favorable and thermodynamically more stable than its decomposition into the individual elements or binary compounds [76]. The resulting negative formation energy for $YHgMnH_6$ confirms that this phase is thermodynamically stable against decomposition into its constituent elements. A positive formation enthalpy (17.032 Ry/atom) indicates that $YZnMnH_6$ is not the ground-state phase at 0 K with respect to decomposition into its elemental constituents. However, the absence of imaginary phonon modes and satisfaction of the Born stability criteria demonstrate that the structure is a metastable local minimum and could potentially be synthesized under suitable conditions. This framework is protected by a kinetic activation energy barrier that prevents spontaneous structural decomposition.

In addition to formation energies, the cohesive energies (E_{Co}) is referred to as the energy to bind the constituent atoms for perovskites $YXMnH_6$ (X = Hg, and Zn), are computed to determine structural stability by the relation (Equation 27) [77]:

$$E_{Co}^{\text{YXMnH}_6} = \frac{\left(E_Y + E_X + E_{Mn} + 3E_{H_2}\right) - E_{total}^{\text{YXMnH}_6}}{N} \tag{27}$$

Where $E_{total}^{\text{YXMnH}_6}$ signifies total energy of the system and $E_Y, E_X, E_{Mn}, and\, E_{H_2}$ signifies the isolated atom energies. N represents the total number of atoms. A higher positive cohesive energy means that the material is more stable, and it has strong atom-to-atom bonds within the material [78]. From Table 5, it can

TABLE 5 Cohesive energies (E_{Co}, Ry/atom) and decomposition energy (ΔH_d, Ry/atom) for both pathway 1 and 2 of perovskites hydrides $YXMnH_6$ (X = Hg, Zn).

ΔH_d		E_{Co}	Compounds
Pathway 2	Pathway 1		
0.0514	0.0386	0.191	$YHgMnH_6$
−17.07	−16.90	−16.89	$YZnMnH_6$

be seen that $YHgMnH_6$ (0.191 Ry/atom) is structurally more stable than the structure $YZnMnH_6$ (−16.89 Ry/atom).

Perovskite hydrides have recently been attracting significant interest in solid-state storage materials because of their high storage density and low latency. Therefore, it is important to measure the hydrogen storage capacity ($C_{wt\%}$) of these materials, which is expressed in weight percentage (wt%) units [79]. It shows how much hydrogen may be held per unit weight of a certain substance. To evaluate the possible use of these materials for practical hydrogen storage, the hydrogen storage capacity ($C_{wt\%}$) of the examined compounds $YXMnH_6$ (X = Hg or Zn), and for the first time is determined using the following expression (Equation 28).

$$C_{wt\%} = \left(\frac{n_H \times m_H}{m_{Host} + n_H \times m_H} \times 100 \right)\% \tag{28}$$

The molar masses of the host compound (M_{YHgMn} = 344.433 g/mol and M_{YZnMn} = 209.233 g/mol) are represented by m_{Host} in this equation, whereas the molar masses of hydrogen (M_H = 1.008 g/mol) are represented by m_H. The number of hydrogen atoms per formula unit is indicated by n_H. The gravimetric hydrogen storage capacities of the analyzed perovskites represent in Table 6 and compared to some typical hydride perovskites previously used for hydrogen storage. $YZnMnH_6$ shows a better gravimetric hydrogen capacity of 2.81 wt%, higher than the gravimetric hydrogen capacities of $CsBaGaH_6$ (1.75 wt%) [19], Ba_2VH_6 [80], $NaScOsH_6$ (2.29 wt%) [50], $KSrIrH_6$ (1.86 wt%) [26] and $NaBaRhH_6$ (2.25 wt%) [48]. However, it is lower than some other hydride perovskite materials, such as $NaSrCoH_6$ (3.44 wt%) [48], and $NaCaCoH_6$ (4.72 wt%) [18]. This difference in gravimetric hydrogen storage capacity is explained by the effect of the A- and B-site atoms in the hydride perovskite structure, mainly due to the difference in their molar mass.

It is important to evaluate the volumetric storage of $YHgMnH_6$ and $YZnMnH_6$, which strongly correlates with the unit cell volume of the material and refers to the amount of hydrogen stored in a given volume. Thus, the hydrogen storage capacity of our compounds can be calculated via volume as given in Table 6 according to the Equation 29 [77]:

$$\rho_{vol} = \frac{N_H . m_H}{V(L) . N_A} \tag{29}$$

In which N_H is the number of absorbed H atoms, $V(L)$ is the unit cell volume in liters, and N_A is Avogadro's number (N_A = 6.022 $\times 10^{23}$ mol^{-1}). As listed in Table 6, the calculated ρ_{vol} values for $YHgMnH_6$ and $YZnMnH_6$ are 124.31 g H_2/L and 136.57 g H_2/L,

TABLE 6 H_2 storage properties ($C_{wt\%}$, wt%), ρ_{vol}, g. H_2/L), the formation energy (ΔH_f, Ry/atom) and desorption temperature (T_{des}, K) of perovskites hydrides $YXMnH_6$ (X = Hg, Zn) compared to previous theorical studies.

References	T_{des}	ΔH_f	ρ_{vol}	$C_{wt\%}$	Compound
This work	824.44	−0.0821	124.31	1.73	$YHgMnH_6$
This work	_	17.032	136.57	2.81	$YZnMnH_6$
19	577.05	−0.1242	_	1.75	$CsBaGaH_6$
75	130.6	−0.0014	125.0	9.41	$LiMgAlH_6$
80	206.2	−0.0204	_	1.82	Ba_2VH_6
69	816.09	0.0404	132.88	2.81	Li_2PtH_6
85	804.712	−0.0801	125	2.68	$LiRhH_3$

respectively. The higher capacity $YZnMnH_6$ is due to the smaller lattice volume and higher packing density. The larger atomic radius and molar mass of Hg compared to Zn increases the unit cell size, which decreases the ratio of hydrogen to volume. Interestingly, both compounds exceed the U.S. Department of Energy (DOE) target value of 40 g/L [81]. While the small gravimetric capacities of the two compounds, 1.73 wt% and 2.81 wt%, respectively, are significant constraints on their usefulness for onboard use in a vehicle, these outstanding materials have high volumetric packing efficiency because they have compact crystal lattices. The high volumetric storage capacity of $YXMnH_6$ presents a promising opportunity in stationary energy applications to overcome gravimetric challenges by storing the maximum amount of hydrogen in a given volume and maximizing the system's space utilization.

Decomposition energy (ΔH_d) of the materials $YXMnH_6$ (X = Hg, and Zn) was studied to suggest alternative synthesis of the materials. Two main decomposition pathways were simulated to assess stability, which represents decomposition to binary halides, and the individual elements. The decomposition equations corresponding are written as:

$$\text{Pathway 1: } \Delta H_d = YH_2 + X + Mn + 2H_2 - YXMnH_6$$

$$\text{Pathway 2: } \Delta H_d = YH_2 + XMn + 2H_2 - YXMnH_6$$

The calculated energies of the decomposition reactions for both paths are shown in Table 5. A positive ΔH_d indicates that the target compound to be formed is energetically more stable than the products of the decomposition reaction [82]. As shown, $YHgMnH_6$ compound exhibit positive decomposition energies 0.0386 Ry/atom (Pathway 1) and 0.0514 Ry/atom (Pathway 2). While $YZnMnH_6$ shows negative values. The results obtained definitely indicate that the $YHgMnH_6$ compounds are thermodynamically stable compared to $YZnMnH_6$ and not prone to decomposing into these competitive phases.

Lastly, the desorption temperature (T_{des}) is crucial to calculate an amount of temperature that is desirable to eject the stored hydrogen from the material surface [83]. The desorption temperature of $YHgMnH_6$ and $YZnMnH_6$ is calculated in the

Equation 30 [84]:

$$T_{des} = \left| \frac{\Delta H}{\Delta S} \right| \quad (30)$$

In which ΔH is related to the enthalpy change obtained by using Equation 26, and ΔS is the entropy change for hydrogen desorption, a typical value of ΔS is taken to be 130.7 J/mol.K [25]. The desorption temperatures shown in Table 6 indicate that $YHgMnH_6$ has a value of 824.44 K, whereas $YZnMnH_6$ is unfeasible for owning positive ΔH. However, T_{des} value adjusted by controlling the doping level and strain for making our compound suitable for hydrogen storage applications [85].

4 Conclusion

This study investigates, for the first time, the electronic, optical, structural, mechanical, and thermodynamic characteristics of the complex hydrides $YXMnH_6$ (X = Hg, Zn) for H_2 storage applications using first-principles calculations based on density functional theory (DFT). WIEN2k and Quantum ESPRESSO (QE) simulation packages were performed for computations. The results confirm that all compounds crystallize cubically. The indirect-bandgap semiconducting behavior of $YHgMnH_6$ and $YZnMnH_6$ compounds has also been validated by electronic band structure investigation, utilizing both GGA-PBE and mBJ-GGA functionals. The obtained elastic constants ensure the mechanical stability of the compounds, since they satisfy the Born criteria. The calculated B/G and Poisson's ratios of $YZnMnH_6$ show brittle behavior. However, $YHgMnH_6$ is also classified as brittle, and the fact that it comes close to the ductile-brittle boundary (1.75) suggests a slight departure from the deformation characteristics. Further, the presence of elastic anisotropy implies that there are significant differences in the mechanical properties along different crystallographic directions. The optical study, including the complex dielectric function and the absorption coefficient, reveals that $YHgMnH_6$ has a better optical response in the UV region. These peaks in absorption and reflectivity in the strong UV response suggest the potential for integrated optoelectronic devices. Interestingly, the calculated volumetric and gravimetric hydrogen storage capacities are 124.31 g H_2/L (1.73 wt%) for $YHgMnH_6$ and 136.57 g H_2/L (2.81 wt%) for $YZnMnH_6$. It must be noted that, although the Mercury-based hydrides have excellent structure and electronic properties as hydrogen storage systems, their use is practically limited by the high toxicity and environmental hazards of Mercury. Thus, our results point to the theoretical potential of these materials, however, any future experimental synthesis should take care to follow safety precautions or to explore less toxic materials with the same structure framework. Our research provides vide a critical benchmark for this type of hydride, suggesting that further substitution with lighter elements (for example, Li or Na) could significantly enhance hydrogen storage while maintaining structural integrity as observed in this study.

In order to continue, our future work will focus on the synthesis and experimental confirmation of these compounds, likely *via* high-pressure or mechanochemical processes. To fully assess energy efficiency, further computational work is required to estimate hydrogen desorption enthalpy and explore catalytic doping to accelerate sorption kinetics. Overall, this study not only introduces a novel class of high-performance hydrogen storage materials, but it also offers a comprehensive roadmap for advancing generation of sustainable energy.

Data availability statement

The raw data supporting the conclusions of this article will be made available by the authors, without undue reservation.

Author contributions

DS: Data curation, Formal Analysis, Investigation, Methodology, Resources, Software, Writing – original draft, Writing – review and editing. MA-J: Conceptualization, Formal Analysis, Investigation, Methodology, Project administration, Supervision, Validation, Visualization, Writing – review and editing. AH: Data curation, Formal Analysis, Methodology, Conceptualization, Software, Visualization, Writing – review and editing. HM: Data curation, Formal Analysis, Investigation, Methodology, Resources, Writing – original draft, Validation.

Funding

The author(s) declared that financial support was not received for this work and/or its publication.

Conflict of interest

The author(s) declared that this work was conducted in the absence of any commercial or financial relationships that could be construed as a potential conflict of interest.

Generative AI statement

The author(s) declared that generative AI was not used in the creation of this manuscript.

Any alternative text (alt text) provided alongside figures in this article has been generated by Frontiers with the support of artificial intelligence and reasonable efforts have been made to ensure accuracy, including review by the authors wherever possible. If you identify any issues, please contact us.

Publisher's note

References

1. Perera F, Nadeau K. Climate change, fossil-fuel pollution, and children's health. *New Engl J Med* (2022) 386(24):2303–14. doi: 10.1056/NEJMRA2117706

2. Le TS, Nguyen TN, Bui DK, Ngo TD. Optimal sizing of renewable energy storage: a techno-economic analysis of hydrogen, battery and hybrid systems considering degradation and seasonal storage. *Appl Energy* (2023) 336(Apr):120817. doi: 10.1016/j.apenergy.2023.120817

3. Tian G, Li Z, Zhang C, Liu X, Fan X, Shen K, et al. Upgrading CO2 to sustainable aromatics *via* perovskite-mediated tandem catalysis. *Nat Commun* (2024) 15(1):3037. doi: 10.1038/s41467-024-47270-z

4. Chowdhury MS, Rahman KS, Chowdhury T, Nuthammachot N, Techato K, Akhtaruzzaman M, et al. An overview of solar photovoltaic panels' end-of-life material recycling. *Energy Strategy Rev* (2020) 27:100431. doi: 10.1016/J.ESR.2019.100431

5. Ishaq H, Dincer I, Crawford C. A review on hydrogen production and utilization: challenges and opportunities. *Int J Hydrogen Energy* (2022) 47(62):26238–64. doi: 10.1016/J.IJHYDENE.2021.11.149

6. Kumar S, Rathore K. Renewable energy for sustainable development goal of clean and affordable energy. *Int J Mater Manufacturing Sustainable Tech* (2023) 2(1):1–15. doi: 10.56896/IJMMST.2023.2.1.001

7. Ali M, Bibi Z, Younis M, Mubashir M, Iqbal M, Usman Ali M, et al. An accurate prediction of electronic structure, mechanical stability and optical response of BaCuF3 fluoroperovskite for solar cell application. *Solar Energy* (2024) 267:112199. doi: 10.1016/J.SOLENER.2023.112199

8. Züttel A. Hydrogen storage methods. *Naturwissenschaften* (2004) 91(4):157–72. doi: 10.1007/S00114-004-0516-X

9. Hosseini SE, Wahid MA. Hydrogen production from renewable and sustainable energy resources: promising green energy carrier for clean development. *Renew Sustainable Energy Rev* (2016) 57:850–66. doi: 10.1016/J.RSER.2015.12.112

10. Abdin Z, Zafaranloo A, Rafiee A, Mérida W, Lipiński W, Khalilpour KR. Hydrogen as an energy vector. *Renew Sustainable Energy Rev* (2020) 120:109620. doi: 10.1016/J.RSER.2019.109620

11. Lee SY, Lee JH, Kim YH, Kim JW, Lee KJ, Park SJ. Recent progress using solid-state materials for hydrogen storage: a short review. *Processes* (2022) 10(2):304. doi: 10.3390/PR10020304

12. Siddique A, Khalil A, Almutairi BS, Tahir MB, Sagir M, Ullah Z, et al. Structures and hydrogen storage properties of AeVH3 (Ae = Be, Mg, Ca, Sr) perovskite hydrides by DFT calculations. *Int J Hydrogen Energy* (2023) 48(63):24401–11. doi: 10.1016/J.IJHYDENE.2023.03.139

13. Khan W, Masood MK. The investigation of rubidium-based hydrides for hydrogen storage application: density functional theory study. *Mater Sci Semicond Process* (2024) 173:108149. doi: 10.1016/J.MSSP.2024.108149

14. Ghebouli B, Ghebouli MA, Fatmi M. First-principles study of structural, elastic, electronic and optical properties of perovskites XCaH3 (X = Cs and Rb) under pressure. *Solid State Sci* (2010) 12(4):587–96. doi: 10.1016/j.solidstatesciences.2010.01.009

15. Shah MAH, Alam MA, Hossain A, Hossain MF, Nuruzzaman M, Parvin F, et al. Hydrostatic pressure on XLiH3 (X = Ba, Sr, Ca) perovskite hydrides: an insight into structural, thermo-elastic and ultrasonic properties through first-principles investigation. *Solid State Commun* (2021) 328(Apr):114222. doi: 10.1016/j.ssc.2021.114222

16. Surucu G, Candan A, Gencer A, Isik M. First-principle investigation for the hydrogen storage properties of NaXH3 (X= Mn, Fe, Co) perovskite type hydrides. *Int J Hydrogen Energy* (2019) 44(57):30218–25. doi: 10.1016/J.IJHYDENE.2019.09.201

17. Siddique A, Khalil A, Almutairi BS, Bilal Tahir M, Ahsan T, Hannan A, et al. Structural, electronic, mechanical and dynamical stability properties of LiAH3 (A = Sc, Ti & V) perovskite-type hydrides: a first principle study. *Chem Phys* (2023) 568(Apr):111851. doi: 10.1016/j.chemphys.2023.111851

18. Hosen A, Nemati-Kande E, Alkhaldi HD, Mousa AA, Akremi A, Boukhris I, et al. Designing high-capacity hydrogen storage materials: DFT insights into Ca-based complex hydrides MCaM′H6 (M = Li, Na; M′= Co, Rh, ir). *J Mater Res Technology* (2025) 36:8688–97. doi: 10.1016/j.jmrt.2025.05.112

19. Mohammad NFAS, Nemati-Kande E, Mousa AA, Abu-Jafar MS, Hosen A, Alshamari A, et al. Exploring the structural stability, optoelectronic characteristics, and H2 storage efficiency of ZBaGaH6 (Z = K, Rb, Cs) complex hydrides: a first-principles insight. *Electrochim Acta* (2025) 542(Dec):147467. doi: 10.1016/j.electacta.2025.147467

20. Rkhis M, Laasri S, Touhtouh S, Hlil E, Bououdina M, Ahuja R, et al. Engineering the hydrogen storage properties of the perovskite hydride ZrNiH3 by uniaxial/biaxial strain. *Int J Hydrogen Energy* (2022) 47(5):3022–32. doi: 10.1016/j.ijhydene.2021.10.237

21. Garara M, Benzidi H, Abdellaoui M, Lakhal M, El kenz A, Benyoussef A, et al. Hydrogen storage properties of perovskite-type $MgCoH_3$ under strain effect. *Mater Chem Phys* (2020) 254(Nov):123417. doi: 10.1016/j.matchemphys.2020.123417

22. Hosen A, Dahliah D, AlShaikh Mohammad NF, Mousa AA, Abu-Jafar MS. A computational study on the comparative analysis of tetragonal complex metal hydride Q2FeH5 (Q = Mg, Ca, Sr) for hydrogen storage applications. *Int J Hydrogen Energy* (2025) 102:348–59. doi: 10.1016/j.ijhydene.2025.01.042

23. Hussain S, Kumar A, Alsubih M, Makasana J, Ballal S, Jayabalan K, et al. Study of structural, electronic, optical, mechanical, and thermodynamic properties of novel perovskite Mg2CaGeH6 material for hydrogen storage applications: computational predictions. *Int J Hydrogen Energy* (2025) 149(Jul):150078. doi: 10.1016/j.ijhydene.2025.150078

24. Dai Q, Tang TY, Liang QQ, Chen ZQ, Wang Y, Tang YL. Exploration of A2BH6(A = K, Rb; B = Ge, Sn) hydrides for hydrogen storage applications: a first principles study. *Int J Hydrogen Energy* (2024) 92:769–78. doi: 10.1016/j.ijhydene.2024.10.324

25. Caid M, Deligöz E, Ozisik H, Rached H, Rached D, Mansour H, et al. Exploring the potential of Rb2XYH6 (XY = AlTl, NaGa, NaTl) double perovskite hydrides for hydrogen storage and energy harvesting *via* DFT. *Int J Hydrogen Energy* (2025) 182:151797. doi: 10.1016/J.IJHYDENE.2025.151797

26. Chelh A, akenoun B, Dahbi S, Ez-Zahraouy H, Elghmaz EA, EL-Gawaad NA, et al. First-Principles study of the stability, physical properties, and molecular dynamics in KSrZH6 (Z = Rh, ir) for hydrogen storage applications. *Adv Theor Simul.* (2025) 8:e00622. doi: 10.1002/adts.202500622

27. Abdulla HT, Abdulkareem NA, Sadiq D, Abdulhussein HA, Hosen A, Al-Ahmed ZAM, et al. Computational assessment of novel KBaMH6 (M = Co, Rh, Ir) complex hydrides for hydrogen storage applications: a DFT and AIMD insight. *Int J Hydrogen Energy* (2025) 192(Nov):152224. doi: 10.1016/J.IJHYDENE.2025.152224

28. Schwarz K, Blaha P. Solid state calculations using WIEN2k. *Comput Mater Sci* (2003) 28(2):259–73. doi: 10.1016/S0927-0256(03)00112-5

29. Blaha P, Schwarz K, Tran F, Laskowski R, Madsen GKH, Marks LD. WIEN2k: an APW+lo program for calculating the properties of solids. *J Chem Phys* (2020) 152(7):74101. doi: 10.1063/1.5143061

30. Blaha P, Schwarz K, Sorantin P, Trickey SB. Full-potential, linearized augmented plane wave programs for crystalline systems. *Comput Phys Commun* (1990) 59(2):399–415. doi: 10.1016/0010-4655(90)90187-6

31. Hohenberg P, Kohn W. Inhomogeneous electron gas. *Phys Rev* (1964) 136(3B):B864–B871. doi: 10.1103/PhysRev.136.B864

32. Giannozzi P, Baroni S, Bonini N, Calandra M, Car R, Cavazzoni C, et al. Quantum ESPRESSO: a modular and open-source software project for quantum simulations of materials. *J Phys Condensed Matter* (2009) 21(39):395502. doi: 10.1088/0953-8984/21/39/395502

33. Perdew JP, Burke K, Ernzerhof M. Generalized gradient approximation made simple. *Phys Rev Lett* (1996) 77(18):3865–8. doi: 10.1103/PhysRevLett.77.3865

34. Tran F, Blaha P. Accurate band gaps of semiconductors and insulators with a semilocal exchange-correlation potential. *Phys Rev Lett* (2009) 102(22):226401. doi: 10.1103/PhysRevLett.102.226401

35. Methfessel M, Paxton AT. High-precision sampling for Brillouin-zone integration in metals. *Phys Rev B* (1989) 40(6):3616–21. doi: 10.1103/PhysRevB.40.3616

36. D Murnaghan BF. On the theory of the tension of an elastic cylinder. *Proc Natl Acad Sci* (1944) 30(12):382–4. doi: 10.1073/PNAS.30.12.382

37. Jamal M, Bilal M, Ahmad I, Jalali-Asadabadi S. IRelast package. *J Alloys Compd* (2018) 735:569–79. doi: 10.1016/J.JALLCOM.2017.10.139

38. Le Page Y, Saxe P. Symmetry-general least-squares extraction of elastic data for strained materials from *ab initio* calculations of stress. *Phys Rev B* (2002) 65(10):104104. doi: 10.1103/PhysRevB.65.104104

39. Zuo L, Humbert M, Esling C. Elastic properties of polycrystals in the voigt-reuss-hill approximation. *J Appl Crystallogr* (1992) 25(6):751–5. doi: 10.1107/S0021889892004874

40. Kuzmenko AB. Kramers-kronig constrained variational analysis of optical spectra. *Rev Scientific Instr* (2005) 76(8):1–9. doi: 10.1063/1.1979470

41. Giannozzi P, De Gironcoli S, Pavone P, Baroni S. *Ab initio* calculation of phonon dispersions in semiconductors. *Phys Rev B* (1991) 43(9):7231–42. doi: 10.1103/PhysRevB.43.7231

42. D Murnaghan BF. The compressibility of media under extreme pressures. *Proc Natl Acad Sci* (1944) 30(9):244–7. doi: 10.1073/PNAS.30.9.244

43. Camargo-Martínez JA, Baquero R. Performance of the modified Becke-Johnson potential for semiconductors. *Phys Rev B* (2012) 86(19):195106. doi: 10.1103/PhysRevB.86.195106

44. Murtaza H, Munir J, Ain Q, Aldwayyan AS, Ghaithan HM, Ahmed AAA, The hydrogen storage and extraction abilities of cesium-based Perovskite hydrides Cs2TlB′H6 (B′= In, Ga): first-principles calculations. *J Inorg Organomet Polym Mater* (2025) 35(5):3401–14. doi: 10.1007/S10904-024-03463-Z

45. Ahmed M, Fatima R, Bakar A, Orynbassar A, Shynarbek N, Khairy Y. Exploration of hydrides XSrH3(X=Cs,Fr) for hydrogen storage applications: a first principles study. *Int J Hydrogen Energy* (2024) 83:460–71. doi: 10.1016/j.ijhydene.2024.08.076

46. mana Al-Anazy M, Mustafa GM, Zayed O, Younas B, Al-Daraghmeh TM, Alkhaldi ND, et al. Study of alkaline metals hydrides RbXH3 (X = Mg/Ca/Sr/Ba) for green energy and hydrogen storage applications. *Int J Hydrogen Energy* (2024) 78:927–37. doi: 10.1016/j.ijhydene.2024.06.373

47. Saikot MSH, Rafiu R, Apon IA, El-Rayyes A, Rahman MA, Shkir M, et al. First-principles investigation of structural, electronic, optical, mechanical, and phonon properties of Pb- and Sn-based cubic oxide perovskites for optoelectronic applications. *RSC Adv* (2025) 15(46):39071–91. doi: 10.1039/D5RA06065F

48. Alhameedi K, Hosen A, Abdulhussein HA, Al-kirbasee NE, Akremi A, Boukhris I. A systematic computational study on Na-based complex hydrides NaMXH6 (M = Sr, Ba; X = Co, Rh, ir): a promising class of hydrogen storage materials. *Chin J Phys* (2025) 97:1240–54. doi: 10.1016/j.cjph.2025.08.033

49. Murtaza H, Ain Q, Munir J, Albrahee I, Qaid SMH, Aldwayyan AS. Vacancy engineering in Na2LiAlH6: enhancing hydrogen storage for sustainable energy solutions. *Int J Hydrogen Energy* (2025) 142:90–7. doi: 10.1016/j.ijhydene.2025.05.407

50. Hosen A, Sadeghi A, Abdulhussein HA, Nemati-Kande E, Nawaz Khan A, Bekkali H, et al. First-principles insights into NaScQH6 (Q = Fe, Ru, Os): promising high-density hydrogen storage materials. *Int J Hydrogen Energy* (2025) 177:151392. doi: 10.1016/j.ijhydene.2025.151392

51. Hosen A, Islam MR. Exploring A3-xBxAlH6 (A/B=Li, Na, K; x = 0, 1, 2) complex hydrides for efficient hydrogen storage: a systematic computational approach. *Int J Hydrogen Energy* (2025) 151(Jul):150220. doi: 10.1016/j.ijhydene.2025.150220

52. Rhrissi I, Bouhmouche A, Moubah R. Electronic, phonon, mechanical, and optical properties of the XAlH5 (X= Be, Sr, and Ca) hydrides with high hydrogen storage capacity. *Int J Hydrogen Energy* (2025) 117:146–57. doi: 10.1016/j.ijhydene.2025.03.111

53. Usman M, Rehman Ju., Tahir MB, Hussain A, Alrobei H, Alzaid M, et al. First-principles calculations to investigate structural, electronics, optical, and mechanical properties of Bi-based novel fluoroperovskites TBiF3 (T = Hg, Xe) for optoelectronic applications. *Mater Sci Semicond Process* (2023) 160(Jun):107399. doi: 10.1016/J.MSSP.2023.107399

54. Masood MK, Khan W, Bibi S, Munir O, Timilsena S, Kanwal J, et al. The first principles investigation of free-lead perovskite-type hydrides CsXH3 (X = Sc, Y) for hydrogen storage application. *Comput Theor Chem* (2025) 1246:115144. doi: 10.1016/j.comptc.2025.115144

55. Masri HA, Abu-Jafar MS, Mohammad NFA, Essaoud SS. Extensive DFT study of FeMnCrGe quaternary Heusler alloy: structural, elastic, magnetic, optical and thermoelectric properties. *Opt Quan Electron.* (2025) 57(2):139. doi: 10.1007/s11082-024-08029-4

56. Ahmed B, Tahir MB, Sagir M, Dhahri N. Computational screening of Ti-Based YTi3H8 (Y = Na, K and Rb) hydrides for efficient solid-state hydrogen storage system. *Phys Lett Section A: Gen At Solid State Phys* (2025) 538(Apr):130345. doi: 10.1016/j.physleta.2025.130345

57. Akhtar D, Gillani SSA, Zeba I, Ahmed A. A probing ion substitution in computational synthesis of CaLiF3-xHx perovskite: a step towards more refined hydrogen storage systems. *J Energy Storage* (2026) 143:119728. doi: 10.1016/J.EST.2025.119728

58. Usman M, Wu A, Bibi N, Rehman S, Rehman MA, Ahmad S, et al. Hydrogen storage application of Zn-based hydride-perovskites: a computational insight. *Opt Quan Electron.* (2024) 56(9):1478. doi: 10.1007/S11082-024-07399-Z

59. Raza HH, Naeem M, Ali HS, Parveen A, Al-Enizi AM. First-principles investigation of BX3H9 (X = Ca, Sc, Ti) hydrides: structural, electronic, phonon, and hydrogen storage properties. *J Phys Chem Sol* (2025) 205:112800. doi: 10.1016/j.jpcs.2025.112800

60. Laghdas A, Matine A, El Rharib A, Hlal M, Amine A, Laghdas K. First principles analysis of hydrogen storage and release performance of the perovskite type XCrH3: structural, mechanical, optical and thermodynamic behavior. *J Energy Storage* (2025) 132:117862. doi: 10.1016/J.EST.2025.117862

61. Algahtani A, Liaqat M, Amina Sajjad M, Quraishi A, Kamolova N, et al. Exploring the structural, electronic, mechanical, magnetic and optical properties of Cs-based hydride-perovskites CsXH3 (X = Cr, Mn) for hydrogen storage application. *Inorg Chem Commun* (2024) 170:113139. doi: 10.1016/J.INOCHE.2024.113139

62. Parvaiz MM, Khalil A, Elsaeedy HI, Tahir MB, Ayub S, Ullah Z. Extensive screening of novel BaXH3 (X = V, Cr, Co, Ni, Cu, and Zn) perovskites for physical properties and hydrogen storage application: a DFT study. *Int J Hydrogen Energy* (2024) 87:1056–73. doi: 10.1016/j.ijhydene.2024.09.113

63. Khan W, Masood MK, Chaoui K, Sharma R, Ashraf N, Rafique R, et al. First-principles analysis of physical properties of the novel calcium-based hydrides for hydrogen storage application. *Phys Lett A* (2024) 504:129443. doi: 10.1016/J.PHYSLETA.2024.129443

64. Yamçıçıer Ç. Exploring the structural, elastic, phonon, optoelectronics, and thermoelectric properties of tetragonal complex metal hydride X2MgH4 (X=K, Rb, and Cs) compounds for hydrogen storage applications. *Int J Hydrogen Energy* (2023) 48(100):39930–43. doi: 10.1016/j.ijhydene.2023.09.177

65. Bouhadda Y, Rabehi A, Tahar-Chaouche Bezzari S. First-principle calculation of MgH2 and LiH for hydrogen storage. *J Renew Energies* (2007) 10(4):545–555. doi: 10.54966/jreen.v10i4.757

66. AlShaikh Mohammad NF, Abu-Jafar MS, Asad JH, Farout M, Bouhemadou A, Mousa AA, et al. FP-LAPW study of structural, magnetic, electronic, elastic, and thermoelectric properties of CoCrS Half-Heusler compound. *AIP Adv* (2024) 14(4):045207. doi: 10.1063/5.0194416

67. Qaid SMH, Ain Q, Akhtar M, Murtaza H, Ghaithan HM, Ahmed AAA, et al. A theoretical insight into the physical characteristics of double perovskite Rb2TlInBr6 for renewable energy applications. *Cryst Res Technology* (2024) 59(3):2300329. doi: 10.1002/CRAT.202300329

68. Pettifor DG. Theoretical predictions of structure and related properties of intermetallics. *Mater Sci Technology* (1992) 8(4):345–9. doi: 10.1179/MST.1992.8.4.345

69. Islah J, Darkaoui E, Abbassi A, Taj S, Manaut B, Ez-Zahraouy H. Hydrogen storage and optoelectronic properties of lithium-based Li2BH6 (B = Pt, Pd, Ni) free-lead perovskite hydrides: a first-principles investigation. *J Energy Storage* (2025) 138:118707. doi: 10.1016/J.EST.2025.118707

70. Zener CM, Siegel S. Elasticity and anelasticity of metals. *J Phys Colloid Chem* (2002) 53(9):1468. doi: 10.1021/J150474A017

71. Liang QQ, Hu DY, Tang TY, Gao HX, Wu SQ, Li L, et al. First-principles calculations to investigate structural, electronic, optical and thermodynamic properties of anti-perovskite compounds X3OI(X = Na, K, Rb). *J Mater Res Technology* (2023) 22:3245–54. doi: 10.1016/J.JMRT.2022.12.148

72. Hosen A, Mousa AA, Nemati-Kande E, Khan AN, Abu-Jafar MS, Benassi E, et al. Systematic computational screening and design of double perovskites Q2LiMH6 (Q = K, Rb; M = Ga, In, Tl) for efficient hydrogen storage: a DFT and AIMD approach. *Surf Inter* (2025) 67:106608. doi: 10.1016/J.SURFIN.2025.106608

73. Akarchaou EH, Touti R, El Mekkaouy A, Didi Y, Tahiri A, Chtita S. Computational analysis of X2MgTiH6 (X =Li, Na, and K) double perovskite hydride materials for hydrogen storage applications. *Int J Hydrogen Energy* (2025) 161:150644. doi: 10.1016/J.IJHYDENE.2025.150644

74. Archi M, Bajjou O, Rahmani K, Elhadadi B. A comparative ab initio analysis of the stability, electronic, thermodynamic, mechanical, and hydrogen storage properties of SrZnH3 and SrLiH3 perovskite hydrides through DFT and AIMD Approaches. *Int J Hydrogen Energy* (2025) 105:759–70. doi: 10.1016/j.ijhydene.2025.01.312

75. Liu D, Wu L, Cao K, Zeng H, Liu F, Sa R. First-principles insights into LiMgXH6 (X = Al, Ga, In) for hydrogen storage: a comprehensive study of structural stability, electronic, mechanical, and optical properties. *Int J Hydrogen Energy* (2026) 206:153411. doi: 10.1016/j.ijhydene.2026.153411

76. Al S, Cavdar N, Arikan N. Computational evaluation of comprehensive properties of MgX3H8 (X = Sc, Ti and Zr) as effective solid state hydrogen storage materials. *J Energy Storage* (2024) 80:110402. doi: 10.1016/j.est.2023.110402

77. Ayyaz A, Boukhris I, Zaman M, Ali W, Alkhaldi HD, Hakamy A, et al.Computational investigation of double perovskite hydrides Be2XH6 (X = Cu, Zn, Ag, Cd): efficient materials for hydrogen storage technologies. *J Energy Storage* (2026) 162:122104. doi: 10.1016/J.EST.2026.122104

78. Yamçıçıer Ç, Al S, Kürkçü C. Theoretical investigations on structural, electronic, elastic, thermal, optic and hydrogen storage properties of XAlH6 (X= La, Ce, Pr) aluminium hydrides. *Physica B Condens Matter* (2025) 716:417713. doi: 10.1016/J.PHYSB.2025.417713

79. Kumar A, Kumar K, Kumar A, Pathak PK. *Ab* initio insights into Rb- and Cs-based SbPbH6 hydride double perovskites for thermoelectric performance and hydrogen storage. *AIP Adv* (2025) 15(12):125038. doi: 10.1063/5.0306937

80. El Kihel K, El Fatouaki Z, Tahiri A, Idiri M, El Bouziani M. Electronic structure, optical, phonon, mechanical, thermodynamic, and hydrogen storage properties of A2VH6 (A = Ca, Sr, Ba) perovskite hydrides by DFT calculations. *Physica B Condens Matter* (2026) 726:418219. doi: 10.1016/j.physb.2025.418219

81. Rezaie S, Smeulders DMJ, Luna-Triguero A. Enhanced hydrogen storage in gold-doped carbon nanotubes: a first-principles study. *Chem Eng J* (2023) 476:146525. doi: 10.1016/J.CEJ.2023.146525

82. Ahmad MS, Ovi IA, Saiduzzaman M, Al-Ghamdi H, Alsalmi O, Souayeh B, et al. Modulating optoelectronic and photocatalytic performance of novel lead-free K2AlAgX6 (X = F, Cl, Br) double perovskites: a first-principles investigation. *Physica B Condens Matter* (2026) 735:418665. doi: 10.1016/J.PHYSB.2026.418665

83. Archi M, Bajjou O, Rahmani K, Elhadadi B. Investigation of structural, phonon, thermodynamic, electronic, and mechanical properties of non-toxic XZnH3 (X = Li, Na, K) perovskites for solid-state hydrogen storage: a DFT and AIMD approach. *J Energy Storage* (2025) 112(Mar):115492. doi: 10.1016/j.est.2025.115492

84. Zhou Y, Zhou Y, Dong Q, Yang H, Wang Z, Tan J. Hydrogen capacity, desorption temperatures, and bonding characteristics of MgTMH (TM = Fe, Ru, Os, Mn, Tc, Re) hydrides. *J Energy Storage* (2026) 150:120336. doi: 10.1016/J.EST.2025.120336

85. Waqdim A, Agouri M, Ouhenou H, Fatihi H, Abbassi A, Taj S, et al. Lithium-based hydride perovskites LiXH3 (X = Mo, Tc, Rh) for hydrogen storage applications: a DFT study. *Int J Hydrogen Energy* (2025) 153:150065. doi: 10.1016/J.IJHYDENE.2025.150065